

Dissertation

submitted to the
Combined Faculties for the Natural Sciences and for Mathematics
of the Ruperto-Carola University of Heidelberg, Germany
for the degree of
Doctor of Natural Sciences

presented by

Diplom-Physikerin Marta Zub
Born in Zielona Góra, Poland

Oral examination: 6 Mai 2009

**Galactic Aspects of Gravitational
Microlensing:
High Magnification Events and Stellar Limb-darkening of a Source
Star in the Galactic bulge**

**Referees: Prof. Dr. Joachim Wambsganß
Prof. Dr. Andreas Quirrenbach**

Zusammenfassung

Der Mikro-Gravitationslinseneffekt ist ein wertvolles Werkzeug um extrasolare Planeten um Sterne im Abstand von wenigen kpc zu finden. Die Vermutung eines Planetensignals in den zwei hochverstärkten Mikrolinsenereignissen OGLE 2006-BLG-245 und MOA 2006-BLG-099 veranlasste uns, eine detaillierte Modellierung und Analyse vorzunehmen. Basierend auf dem Vergleich modellierter Einzel- und Doppellinsensysteme zeigten wir, dass die Abweichungen in den beobachteten Lichtkurven nicht durch einen planetaren Begleiter verursacht wurden. Unsere Modellierung und Analyse vier weiterer hochverstärkter Mikrolinsenereignisse veranschaulicht die Möglichkeit, die Detektionseffizienz von Mikrolinsen-Datensätzen hinsichtlich planetarer Begleiter zu untersuchen. Wir analysieren ausserdem das Einzellinsenereignis OGLE-2004-BLG-482, welches dazu benutzt wurde das Helligkeitsprofil des gelinsten Hintergrundsterns im galaktischen Bulge zu messen. Wir führten die Datenreduktion und Analyse hochaufgelöster Lichtkurven dieses Ereignisses durch, welche von den Kollaborationen PLANET, OGLE und MicroFUN mit I -, R - und Klar-Filtern aufgenommen wurden. Wir benutzten ein hochaufgelöstes VLT/UVES-Spektrum, nahe der Maximalverstärkung aufgenommen, um fundamentale Parameter des Quellsterns zu bestimmen, welcher sich als kühler M3-Riesestern mit $T_{\text{eff}} = 3667 \pm 150 \text{ K}$, $\log g = 2.1 \pm 1.0$ entpuppte. Die detaillierte Mikrolinsen-Modellierung der Lichtkurve erlaubte uns Randverdunklungskoeffizienten zu bestimmen und stellt damit eine Diagnose solcher Messungen durch den Mikrolinseneffekt bereit. Der Vergleich unserer Ergebnisse mit Vorhersagen von Modellatmosphären für die entsprechenden stellaren Parameter zeigt, dass diese sehr gut sowohl mit den linearen Randverdunklungsgesetzen als auch mit alternativen Randverdunklungsprofilen, gewonnen aus einer Hauptkomponentenanalyse von ATLAS-Modellen von Sternatmosphären, übereinstimmen.

Abstract

Gravitational microlensing provides a powerful tool to search for extrasolar planets of stars at distances of order of several kpc. The suspicion of a planetary signal in the two high magnification events OGLE 2006-BLG-245 and MOA 2006-BLG-099 led us to perform a detailed modelling and analysis of those two events. Based on the comparison of single-lens and binary-lens models, we demonstrate that the observed light curve deviations are not caused by a planetary companion. Our modelling and analysis of four other high magnification events illustrate the possibility to study detection efficiencies of microlensing data sets to planetary companions. We also present a detailed study of the single-lens OGLE 2004-BLG-482 microlensing event, used to measure the brightness profile of the background lensed star located in the Galactic bulge. We performed data reduction and analysis of well sampled observations of this event obtained by the PLANET, OGLE and MicroFUN collaborations in the I , R and clear filters. We also used a high resolution spectrum obtained with VLT/UVES close to the peak of the light curve to determine the fundamental parameters of the source star, that we find to be a cool red M3 giant with $T_{\text{eff}} = 3667 \pm 150 \text{ K}$, $\log g = 2.1 \pm 1.0$. We then performed a detailed microlensing modelling of the light curve to measure linear limb-darkening coefficients and to provide new diagnostics of such measurements through microlensing. We compare our results to model-atmosphere predictions based on limb-darkening coefficients for the corresponding stellar parameters. Our limb-darkening measurements agree very well with predictions of the model atmosphere, for both linear limb-darkening laws and alternative limb-darkening profiles based on a principal component analysis of ATLAS stellar atmosphere models.

Contents

1	Introduction	3
2	A Review of Gravitational Lensing	5
2.1	Gravitational lensing	5
2.2	The lens equation	5
2.3	The gravitational microlensing effect	8
2.4	Source flux magnification	9
2.5	Microlensing light curves	10
2.6	Binary lenses	11
2.7	Critical curves and caustics	13
2.8	A finite source effect	13
2.8.1	Limb darkening	13
3	Microlensing Data Collection, Analysis and Photometry	15
3.1	OGLE and MOA Microlensing Surveys	15
3.2	Microlensing Follow-up Networks: PLANET and MicroFUN	16
3.3	Photometry and Analysis Techniques	17
3.3.1	Method of Photometry	18
3.3.2	Data Fitting and Minimisation Methods	19
3.4	Red Clump Giants Method	21
4	Planet Detection through Microlensing	23
4.1	Planetary Microlensing	23
4.2	High Magnification Events	24
4.3	Analysis of 2006 High Magnification Events	25
4.3.1	Selection of 2006 High Magnification Events	25
4.3.2	PSPL models of 2006 High Magnification Events	26
4.4	Modelling of OGLE 2006-BLG-245	31
4.5	MOA 2006-BLG-099	35
4.6	Conclusion on the 2006 High Magnification Events	39
5	A Detailed Study of Extended Source Event: OGLE 2004-BLG-482	41
5.1	Introduction	41
5.2	Photometry – Data Reduction and Analysis	43
5.3	Linear limb-darkening formalism	44
5.4	Modelling	46

5.4.1	Single-lens, extended-source models	46
5.4.2	Fitting data	47
5.4.3	Estimates of the lens properties	48
5.5	Calibrated colour-magnitude diagram	49
5.6	Source star properties from the photometry and spectroscopy	52
5.6.1	Conclusion on the source MK type and parameters	54
5.7	Discussion of the linear limb-darkening coefficients	58
5.8	Principal Components Analysis	59
5.9	Summary and Conclusion	60
6	Conclusions and Prospects	65
	Publications	67
	List of figures	69
	Bibliography	73
	Acknowledgements	77

Chapter 1

Introduction

In 1915, the theory of General Relativity by Einstein brought for the first time the proof that a massive body could influence the path of light rays. Some of the most popular manifestation of light deflection are the images of distant galaxies which are distorted into giant luminous arcs. “Gravitational lensing” has since become a very fruitful branch of astrophysics, revealing the presence of dark objects *via* their mass, or magnifying the flux of objects at cosmological distances, such as quasars (e.g. Walsh et al. 1979, for the first observed lensed quasar, Q 0957 + 561A,B).

In 1936, Einstein considered a configuration where two stars in the Milky Way are almost exactly aligned with an observer, and found that the background star would be seen as a bright ring (the “Einstein ring”). However, he concluded that the nowadays so-called “microlensing effect” would never be detectable, because the angular dimension of the Einstein ring is much too small (around half of a milliarcsec). But fifty years later, in 1986, Paczyński published a fundamental article where he proposed a strategy which allow the detection of microlensing events toward the Magellanic Clouds. Shortly after, Mao & Paczyński (1991) demonstrated that observing in the direction of the Galactic bulge would also lead to detectable microlensing events. Although a challenging experiment, two main collaborations formed to check these ideas, EROS and MACHO, and succeeded in 1993 in observing the first ever microlensing events (Alcock et al. 1993; Aubourg et al. 1993).

Another important conclusion of Mao & Paczyński (1991) was that by probing the whole dark content of the Galactic disc, the microlensing technique was also able to detect very small objects, such as extrasolar planets. Once again, predictions were confirmed, and in 2003, the first planet detected by microlensing (MOA 2003-BLG-53 / OGLE 2003-BLG-235, Bond et al. 2004) provided the evidence of the strength of gravitational lensing. In 2005, microlensing was pioneer in unveiling a new class of planets, the now on so-called “Super-Earths”, by the discovery of OGLE 2005-BLG-390Lb, a rocky and icy $\sim 5.5 M_{\oplus}$ planet. These rocky planets of mass around $2 - 20 M_{\oplus}$ are currently major targets of planet search projects. In 2008, microlensing has confirmed its potency to discover very low-mass planets with the detection of MOA-2007-BLG-192Lb (Bennett et al. 2008), a $\sim 3.3 M_{\oplus}$. All the planets discovered by microlensing are located at several kpc, where no other method is able to probe the planet population.

Galactic gravitational microlensing is also one of a few techniques, together with interferometry, transiting extrasolar planets and eclipsing binaries to measure brightness profiles. This aspect in stellar astrophysics is very original in the sense it allows to probe the atmosphere of

stars located in the Galactic bulge, in particular red giants.

In this thesis, we have studied two aspects of Galactic gravitational microlensing: high magnification events to detect the presence of extrasolar planets, and measuring the limb-darkening profile of Bulge stars by using the microlensing effect as a tool.

To understand better the lensing phenomenon, we first introduce in Chapter 2 the important concepts which will enter in the discussion throughout the thesis. The data reduction process using the difference imaging technique is presented in Chapter 3. The PLANET collaboration of which I am a member and its world-wide network of telescopes are also described. In Chapter 4, we introduce binary and planetary microlensing, and discuss in more detail the case of high magnification events to search for extrasolar planets. The core of the chapter is dedicated to the analysis of six promising high magnification events from the observational season 2006, including two interesting candidates which were suspected to hide a planetary signal. In Chapter 5, we perform a detailed analysis of the microlensing event OGLE 2004-BLG-482, to derive precise limb-darkening measurements of the background giant bulge star, that we have compared to stellar atmosphere models. Such microlensing are relatively rare, but contain unique information of stellar atmospheres and opportunity to test atmosphere models. We finally summarise and conclude in Chapter 6, and underline some of the most promising goals that microlensing can achieve in the future, and how.

Chapter 2

A Review of Gravitational Lensing

We hope this chapter acquaints with a few important questions of gravitational lensing phenomenon and presents a briefly review of them.

2.1 Gravitational lensing

A light ray that passes a massive object, undergoes the deflection due to the gravitational potential of that mass. The most simple case of lens is a point with mass M which gravity at a distance r is described by the Newtonian potential

$$\Phi = -\frac{GM}{r} = -\frac{GM}{\sqrt{u^2 + z^2}}. \quad (2.1)$$

Assuming the spherically symmetry of a lens object, for the impact parameter u of light ray much larger than the Schwarzschild radius of lens mass, the deflection angle $\tilde{\alpha}$ is small. Thus the $\tilde{\alpha}$ can be approximated by integration along unperturbed ray z (see Fig. 2.1) which yields

$$\tilde{\alpha}(u) = \frac{4GM(u)}{c^2} \frac{1}{u}, \quad (2.2)$$

where G is the gravitational constant, $M(u)$ is the deflecting mass enclosed within radius u and u is the impact parameter which indicates the minimum approach distance to the object of M mass and c is the speed of light.

Most of light deflection is assumed to occur within the distance z which is much smaller than these ones between an observer and lens and between a lens and source. Thus the lens can be considered a thin sheet and in the plane of it the lens mass distribution is projected (the *thin-lens approximation*). The mass of lens sheet is characterised by its surface mass density Σ

$$\Sigma(\vec{u}) = \int \rho(\vec{u}, z) dz, \quad (2.3)$$

2.2 The lens equation

To imagine how the gravitational lensing phenomenon happens, the geometric description of it with a single lens illustrated in Fig. 2.2 can be helpful. From this sketch using the Euclidean

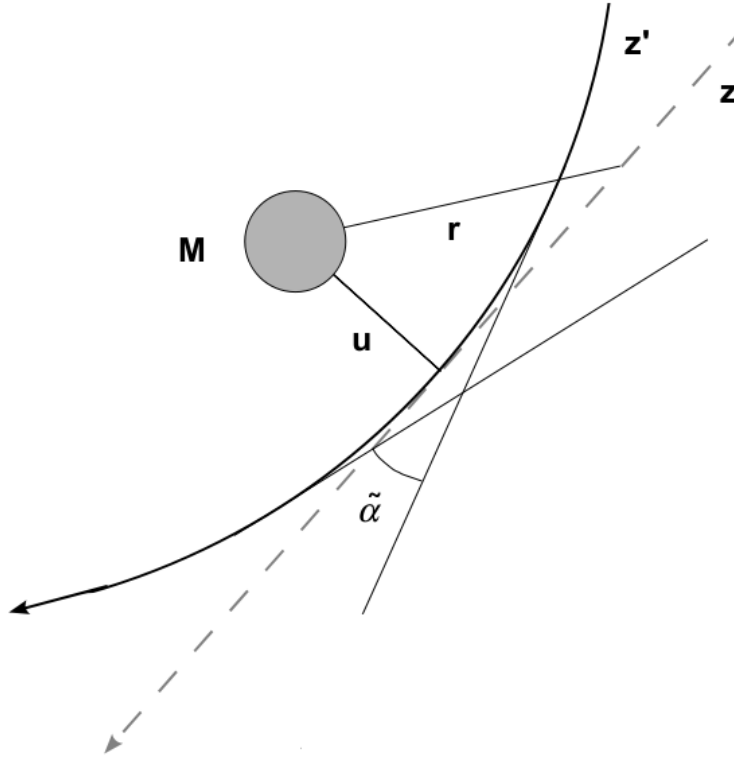


Figure 2.1: In the vicinity of the mass M , the unperturbed ray z (dashed line) and the perturbed one z' (solid curve) pass the lens M at the same approach distance u . Since most of the deflection occurs very close to the lens, the path of perturbed ray can be approximated by two unperturbed ones (solid lines by angle $\tilde{\alpha}$).

relation: angular separation = angle \times distance ¹, it is seen that

$$\theta D_S = \beta D_S + \tilde{\alpha} D_{LS}. \quad (2.4)$$

The deflection angle $\tilde{\alpha}$ depends on the mass distribution of a lens and the impact distance of the light ray. For the reduced deflection angle $\vec{\alpha} = \frac{D_{LS}}{D_S} \tilde{\alpha}$, it is translated into

$$\vec{\beta} = \vec{\theta} - \vec{\alpha}(\vec{\theta}). \quad (2.5)$$

The obtained equation (2.5) is called *the lens equation*. In general, this relation is nonlinear which makes possible to observe multiple images at the positions $\vec{\theta}$ corresponding to a single source at the angular separation of $\vec{\beta}$. Assuming a spherically symmetric lens, the lens equation can be expressed

$$\beta(\theta) = \theta - \frac{D_{LS}}{D_L D_S} \frac{4GM(\theta)}{c^2 \theta}. \quad (2.6)$$

¹This relation is sufficiently precise on the distances of our Galaxy scale

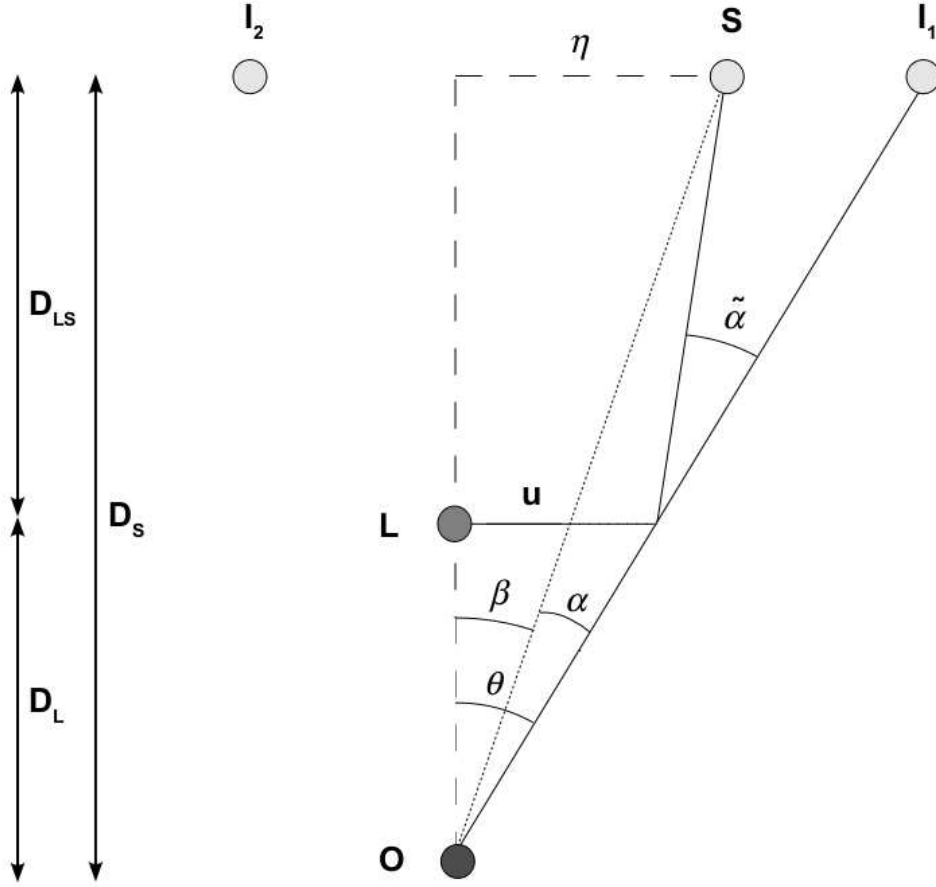


Figure 2.2: Geometric description of gravitational lensing. The light ray emitted from the source S , located at the distance η from the optical axis is detected by the observatory O . Passing the lens L at the approach distance ξ (the impact parameter) it is deflected by an angle $\tilde{\alpha}$. Due to this act two images I_1 and I_2 are created. The angular separations of the source S and the image I_1 from the optical axis are indicated by β and θ , respectively. The lens takes place at the distance D_L and the source is located at the distance D_S . The lens-source distance is D_{LS} .

For a scenario when a source, lens and an observer are exactly on the optical axis (*i.e.* $\beta = 0$), an image is created as a ring. Its angular radius, the so called *Einstein ring radius* (Chwolson 1924; Einstein 1936) is given by

$$\theta_E = \sqrt{\frac{4GM(\theta_E)}{c^2} \frac{D_{LS}}{D_L D_S}}. \quad (2.7)$$

This quantity is the unit to which all length and time scales in gravitational lensing are normalised. Thus the lens equation for a point mass lens, using the Einstein radius Eq. (2.7) can be rewritten in the form

$$\beta = \theta - \frac{\theta_E^2}{\theta}. \quad (2.8)$$

Solving this quadratic equation the positions of images are obtained

$$\theta_{\pm} = \frac{1}{2} \left(\beta \pm \sqrt{\beta^2 + 4\theta_E^2} \right). \quad (2.9)$$

The two images take place on opposite sides of the source with the image separation around $2\theta_E$. One stronger magnified image appears outside the Einstein ring (the positive parity image) and the other one fainter inside (the negative parity image).

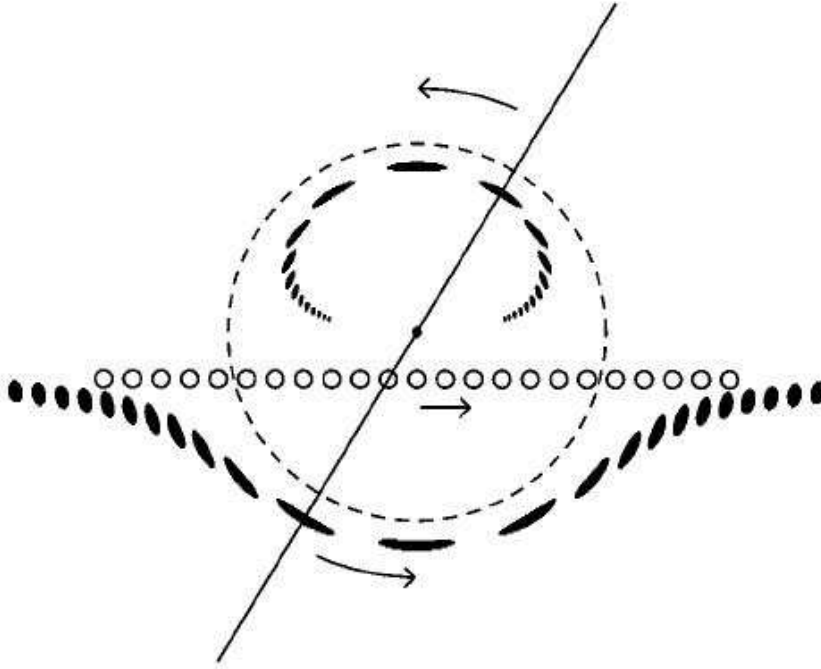


Figure 2.3: The relative tracks of two individual source images are presented. The acting single lens (a black dot in the centre) creates two images of a source. The sequence of more and more elongated black ellipses marks two source images at each stage (a straight line) of source motion. The transverse motion of the source is shown with a series of open circles. The Einstein ring is indicated with a dashed line circle. (from Paczyński (1996a)).

2.3 The gravitational microlensing effect

In the case when a lens object is massive enough (such as a galaxy), the separate images of source can be resolved. This situation is relevant to lens-source distances of the order of Giga parsecs. In the following a lensing system is considered in the Galactic regime. This means the typical lens and source distances are of the order of kilo parsecs and a stellar mass object acts

as a single lens. Typically the lens is a main-sequence star or a dwarf in the foreground Galactic disk or bulge, whereas the source is a giant or main-sequence star usually in the Galactic bulge. A typical Galactic lensing scenario involves a source located at around $D_S = 8$ kpc and a lens at $D_L = 6$ kpc. The associated/corresponding Einstein radius is

$$\theta_E = 2.92 \times \sqrt{\frac{M}{M_\odot} \times \left(\frac{(D_S - D_L)}{D_L D_S} \text{ kpc} \right)} \text{ milliarcseconds.} \quad (2.10)$$

For the mass $M \simeq 0.3M_\odot$ of lensing star which is mainly M dwarf, the Einstein ring radius is $\theta_E \simeq 0.33$ milliarcseconds. In such event the source images are not resolved by the most ground-based telescopes which is called as the *microlensing effect*. However, those images are magnified during acting of gravitational lensing.

2.4 Source flux magnification

The gravitational lens potential causes the distortion of images. The surface brightness of a source is preserved by the gravitational lensing². However the light deflection changes the apparent solid angle of a lensed object. Therefore the total flux from a source image is defined as the ratio between the solid angles of the image and the source. Thus the *magnification* is given by

$$\text{magnification} = \frac{\text{image solid angle}}{\text{source solid angle}} = \frac{\text{area of image}}{\text{area of source}}. \quad (2.11)$$

If k is the number of source images the total magnification A can be analytically expressed by

$$A = \sum_{k=1}^N A_k = \sum_{k=1}^N \frac{1}{|\det J_{i,j}|_k}, \quad (2.12)$$

where the Jacobian $J_{i,j}$ is a transformation matrix of magnification. This matrix transforms positions from the lens plane positions $\mathbf{x} = (x_1, x_2)$ to the source plane $\mathbf{y} = (y_1, y_2)$ is given by

$$J_{i,j} = \frac{\partial y_j}{\partial x_i}. \quad (2.13)$$

The magnifications of the two images are expressed

$$A_{\pm} = \left[1 - \left(\frac{\theta_E}{\theta_{\pm}} \right)^4 \right]^{-1} = \frac{u^2 + 2}{2u \sqrt{u^2 + 4}} \pm \frac{1}{2}, \quad (2.14)$$

where u is the angular separation between a source and a point mass lens scaled in units of the Einstein radius, *i.e.* $u = \beta/\theta_E^2$.

It is good to note that the term of magnification is related to resolved images whereas for unresolved source images is also used in the literature other one, namely amplification.

²due to Liouville's theorem

2.5 Microlensing light curves

Due to relative motion of a source, lens and an observer, the projected impact parameter u changes with time and thus the changes in the source flux can be observed. The characteristic time scale of these variations, so called the *Einstein time* is defined

$$t_E = \frac{D_L \theta_E}{v_\perp}, \quad (2.15)$$

where v_\perp is the transverse velocity of a lens with respect to the source-observer line of sight. It is the time taken for a source to pass/cross the Einstein ring radius. Among the microlensing parameters only t_E is a quantity which provides any information about the physical lens properties. However it still corresponds to a range of lens masses and velocities and distances. Assuming $D_L = 6$ kpc and $D_S = 8$ kpc for a standard microlensing scenario with $v_\perp = 200$ km/s the Einstein time of crossing is of order of

$$t_E \approx 30 \times \sqrt{\frac{M}{M_\odot}} \text{ days}. \quad (2.16)$$

Using Eq. (2.15) the impact parameter u then is given as a time-dependent function

$$u(t) = \sqrt{u_0^2 + \left(\frac{t-t_0}{t_E}\right)^2}, \quad (2.17)$$

where u_0 is the minimum lens-source impact parameter (in units of angular Einstein radius θ_E) at the corresponding time t_0 of maximum amplification.

Then the total measurable amplification of two images for a point-source point-lens configuration can be written as (Paczynski 1986)

$$A(u) = A_+ + A_- = \frac{u^2 + 2}{u \sqrt{u^2 + 4}}. \quad (2.18)$$

In the case when a source, a point lens and an observer are aligned on the optical axis, a source image would be infinitely magnified. In reality the lensed objects have extended sizes thus the magnification remains finite. In general, the highest amplification of the lensed star in a microlensing event involving a single lens is given by

$$A_{\max} \simeq \frac{1}{u_{\min}}, \quad (2.19)$$

for the distance of closest approach $u_{\min} \ll 1$. The magnification reaches $A > 1.34$ when $u \leq 1$.

All these quantity: time of Einstein ring crossing t_E , t_0 and u_0 are the parameters which describe a characteristic, smooth and symmetric light curve for a single lens case, also known as Paczynski light curve. The microlensing light curves from a monitoring of stellar source flux F is expressed as

$$F(t) = A(t) \times F_S + F_B, \quad (2.20)$$

where F_S indicates the unlensed flux of source and F_B is the unresolved flux containing the lens flux and any light of background that is not being lensed. It happens that the latter can include

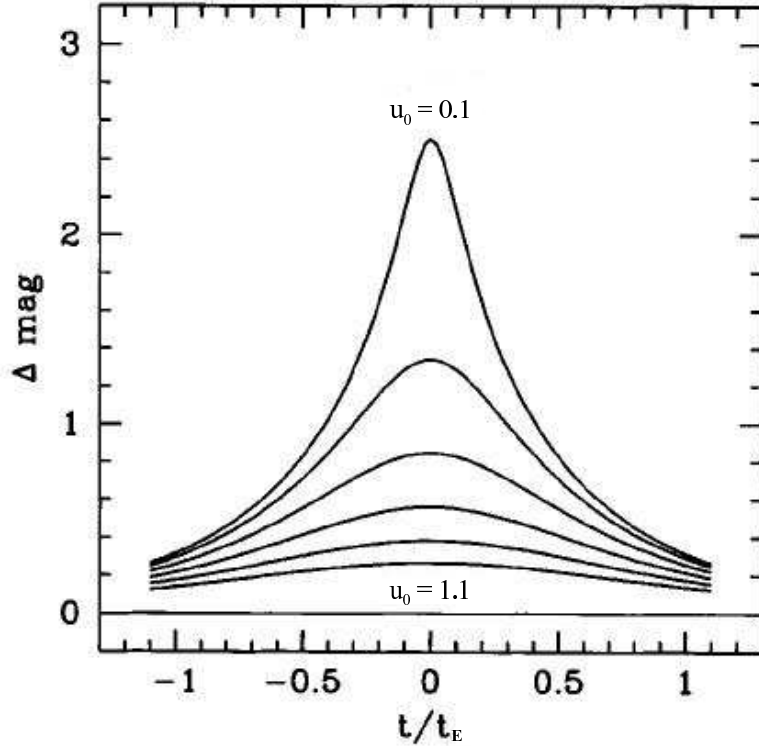


Figure 2.4: The standard point-source, point-lens light curves for different values of the minimum lens-source impact parameter u_0 are presented. (from Paczyński (1996a)).

also the light from the lens companion or/and from the source companion. The contribution of background light in total flux needs to be taken into account in particular in the dense fields as it is the case for the Galactic bulge events.

In fact in the nature, we can observe many different deviations from described theoretical point source point lens light curve. One of them is a binary lens case. This kind of microlensing event will be presented in Sec. 4.1.

2.6 Binary lenses

The described in previous sections a point lens point source case is the most simple out of possible microlensing events.

Considering a system which consists of N lenses, the lens equation can be written as

$$\mathbf{y} = \mathbf{x} - \sum_{k=1}^N m_k \frac{\mathbf{x} - \mathbf{l}_k}{|\mathbf{x} - \mathbf{l}_k|^2}, \quad (2.21)$$

where m_k is a lens mass at the positions \mathbf{l}_k . For a given position in the source plane, \mathbf{y} , the values of \mathbf{x} which fulfil Eq. (2.21), indicate the positions of source images in the lens plane.

If a lens consists of two point mass objects, the caustic shapes and configurations depend on the planet-to-lens mass ratio and the projected planet-lens separation. The central caustic of primary lens (a star) and one (located on the same side of lens as a planet) or two planetary caustics (appear on the opposite lens side) are created depending on a planet position.

A binary lens scenario involves three more parameters: the mass ratio $q = \frac{m_1}{m_2}$ for m_1 and m_2 lensing masses, the source-lens projected separation d , in units of the Einstein ring radius for the total lens mass $m = m_1 + m_2$ and the angle ϕ between the line connecting two lenses and the source trajectory.

Then the lens equation for two lenses can be written as

$$\mathbf{y} = \mathbf{x} - m_1 \frac{\mathbf{x} - \mathbf{l}_1}{|\mathbf{x} - \mathbf{l}_1|^2} - m_2 \frac{\mathbf{x} - \mathbf{l}_2}{|\mathbf{x} - \mathbf{l}_2|^2}, \quad (2.22)$$

where \mathbf{l}_1 and \mathbf{l}_2 indicate the positions of two lens components. The case of planetary binary lens will be presented in Chapter 4.1.

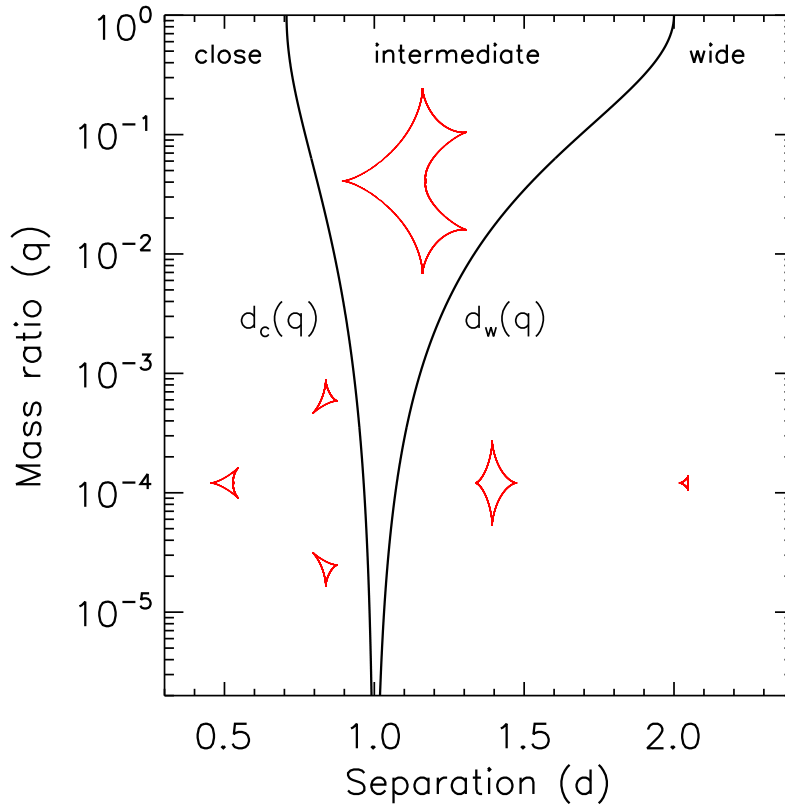


Figure 2.5: The three configurations of caustics created by binary lenses (plotted here for the mass ratio $q = 10^2$). The close binary lens is displayed on the left (for $d = 0.8$), the intermediate binary with a single caustic in the middle part (for $d = 1$) and the wide binary on the right (for $d = 1.6$). (from Cassan (2008)).

2.7 Critical curves and caustics

Gravitational lensing can be considered on the two surfaces: the lens and source planes. Then the projected position of image on the lens plane and the lensed object on the source plane are expressed respectively: $x = \frac{\theta}{\theta_E}$ and $y = \frac{\beta}{\theta_E}$. The set of points for which the Jacobian vanishes, $\det J_{i,j} = 0$ in the lens plane creates smooth curves, known as *critical curves*. The corresponding set of points creates in the source plane a *caustic* which is the structure consisting of the infinite magnification points. Extended caustic patterns formed by lines (fold caustics) that merge at cusps, is created by binary lenses and for a single lens which creates a point-like caustic. The three different topologies of caustics created by binary lenses are presented in Fig. 2.5. The close binary lens involves a central caustic and two off-axis small secondary caustics. The intermediate binary creates a single caustic, whereas the wide binary – a central caustic and an isolated secondary caustic. The caustics are obtained by mapping the critical curves with the lens equation and they indicate regions of large magnification gradients. If a source crosses near a caustic, it can produce very highly magnified images located near the corresponding critical curve in the lens plane. The number of lensed images depends on a source location with respect to the caustic curves.

2.8 A finite source effect

In the vicinity of caustics produced by lenses, the source star flux undergoes a large total magnification. Moreover when the source size is significant, the source becomes differentially magnified around the caustics due to a strong gradient of magnification. The proper motion of lens with respect to the source is in general slow enough to obtain the frequently sampled light curve. This allows to have a high spatial resolution on the source star's surface and hence its brightness profile can be derived from the observations. These so-called finite source effects have proven a powerful tool to probe the limb-darkening of microlensed. The finite source effects occur in two scenarios: caustic crossing (fold or cusp) and in the single lens case. In the latter one the effect of extended source can reveal in the light curve if the angular source size is of order or larger than the angular separation between the source centre and the point-like caustic. In the following we present the analysis and results on the single lens extended source OGLE 2004-BLG-482 event (see: Chapter 5).

2.8.1 Limb darkening

In the reality, stellar disks are not uniformly bright. At the particular circumstances the changes of their intensity from the disk centre to the edge can be observed. This effect known as the limb-darkening is the result of the density and temperature variations in stellar atmosphere and is related to the geometry. The emergent angle of the observed radiation during approaching the disk limb becomes smaller with respect to the stellar surface.

Thus the surface brightness profile I can be written in the form (Claret 2000)

$$\frac{I(\mu)}{I_0} = 1 - \sum_{k=1}^N a_k (1 - \mu^k), \quad (2.23)$$

where I_0 is the intensity at the stellar disk centre, $\mu = \cos(\psi)$ is the cosine of the emergent angle

of light radiation, and a_k , $k = 1/2, 1, 3/2, 2, \dots$ are the wavelength dependent limb-darkening coefficients (LDC). The first approximation of the surface brightness is known as the linear limb-darkening law

$$\frac{I(\mu)}{I_0} = 1 - a(1 - \mu), \quad (2.24)$$

where the linear limb-darkening coefficient a is in range 0..1. This surface brightness profile can be derived by integration over common centre uniform source disks of different radii and different brightness. More details and the results of limb-darkening measurements for a cool red giant are presented in Chapter 5.

We are aware that this briefly review of gravitational lensing questions is far to be comprehensive, therefore the suitable literature is recommended.

Chapter 3

Microlensing Data Collection, Analysis and Photometry

The Galactic microlensing events which are studied in the following were discovered by the OGLE and MOA collaborations and then continuously monitored by the follow-up networks PLANET and MicroFUN. In this chapter we present how photometric data were obtained. We also describe the method which we used to perform the photometry and data reduction. The contents of the current chapter are relevant to the modelling and analysis of high magnification microlensing events presented in Chapter 4 and to the detailed studies of the extended source event OGLE 2004-BLG-482 in Chapter 5.

3.1 OGLE and MOA Microlensing Surveys

Since the duration of planetary signals is very short, a continuous and well-sampled monitoring is necessary. The microlensing observations are carried out in two stages. In the first one, the survey teams such as OGLE and MOA monitor more than $\sim 10^8$ stars towards the Galactic bulge to detect and to announce microlensing events. They use single dedicated telescopes for this purpose. In the second stage follow-up networks alerted by the survey teams lead monitoring of promising targets.

The OGLE collaboration (*Optical Gravitational Lensing Experiment*)¹ (Udalski 2003) carries out continuous observations with the 1.3m Warsaw Telescope located at Las Campanas Observatory (Chile). They measure every few days the apparent brightness of a few million stars. The OGLE-III *Early Warning System* (EWS)² In the following work we use the calibrated data in the *I*- and *V*-band provided by OGLE. Another collaboration – MOA (*Microlensing Observations in Astrophysics*)³ makes observations on dark matter, extrasolar planets and stellar atmospheres at the Mt John Observatory. The second phase of MOA (MOA-II) performs survey observations towards the Galactic bulge to search extrasolar planets through microlensing with a 1.8m telescope in New Zealand. The field of view (FOV) for its camera lens is 2×2 deg and the size of the CCD (charge-coupled device) is $8k \times 10k$ pixel. MOA target fields ($\sim 50 \text{ deg}^2$)

¹<http://ogle.astrouw.edu.pl/>

²<http://ogle.astrouw.edu.pl/ogle3/ews/ews.html>

³<http://www.phys.canterbury.ac.nz/moa/>

are observed with the frequency 10 to 50 times per night and the data are analysed in real-time to send microlensing alerts to follow-up networks.

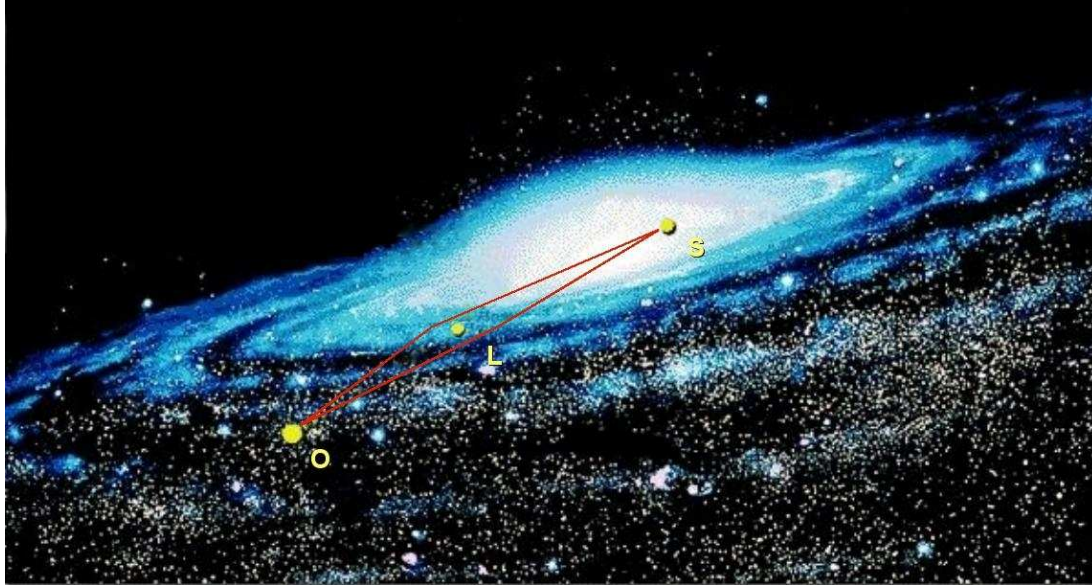


Figure 3.1: A microlensing event scenario with a source star (S) located in the Galactic bulge and a lensing star (L) in the Galactic disc, detected in an observatory (O).

3.2 Microlensing Follow-up Networks: PLANET and MicroFUN

To better sample the light curve of a microlensing event and to avoid data gaps, it is necessary to perform the monitoring by two or more separate teams.

The PLANET collaboration (*Probing Lensing Anomalies NETwork*)⁴ was established in 1995 to monitor microlensing events alerted by OGLE or MOA. For this purpose they use a network of five telescopes located in the Southern Hemisphere on three continents (see Fig. 3.2). Thanks to these locations of detectors, PLANET can perform a “round-the-clock” observation of promising targets. During the Galactic microlensing observing season from April to September when the Bulge is visible from the Southern Hemisphere, PLANET follows alerted events with high precision photometric observations and with high sampling rate (\sim a few times per hour). This activity is supported by daily primary data reduction of ongoing data and daily near-real-time modelling.

Data are collected at the telescopes and reduced online by an image subtraction algorithm (Alard & Lupton 1998) and then they are sent to a central server. The data flow is managed by a current dedicated collaborator, “homebase” who is responsible for the issue of public anomaly alerts and for presenting the different data sets in a consistent way.

In January 2009, PLANET collaboration merged with the team of the Microlensing Follow-Up Network (MicroFUN)⁵. This informal consortium of observers is dedicated to photomet-

⁴<http://planet.iap.fr>

⁵<http://www.astronomy.ohio-state.edu/~microfun/>

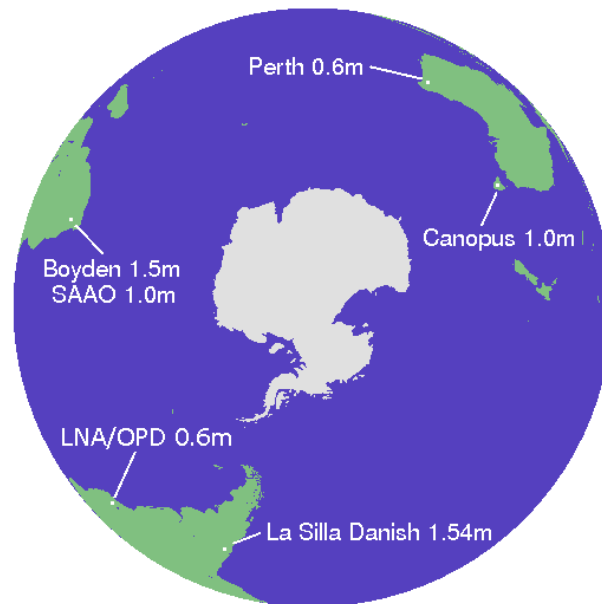


Figure 3.2: The PLANET telescopes that took part in the 2006–2007 PLANET observing campaigns. They are located in Australia, South Africa and South America to provide a round-the-clock monitoring of promising microlensing events in the Galactic bulge.

ric monitoring of interesting microlensing events in the Galactic bulge. Its primary scientific purpose is to observe high magnification microlensing events that give the best potential for detecting extrasolar planets orbiting the lensing star. From the merge both collaborations is expected to improve identification of high magnification events (*i.e.* events which are sensitive to a planetary signal) from photometric data obtained at low magnification. Also, larger telescopes network should provide a better coverage close a light curve peak. Continuous microlensing observations due to 'anomaly alerts' and promising lower magnification events will be lead as well.

Since 2006 I am a member of the PLANET collaboration and besides my work on data reduction, analysis, photometry and modelling I have also performed four observation runs (at the Danish 1.54m telescope in La Silla, Chile 19 nights in July 2006, 13 nights in June 2007, 15 nights in June 2008 and 14 nights in August 2008, at the Elisabeth 1.0m telescope in SAO, South Africa) as well as a homebase shift (one week in August 2007).

3.3 Photometry and Analysis Techniques

All PLANET and MicroFUN photometric data of the OGLE 2004-BLG-482 microlensing event were extracted using different versions of PLANET pipeline designed on the base of image subtraction method that has been developed by Alard & Lupton (1998) and Bramich (2008). The OGLE data set was reduced by OGLE team using their own difference imaging pipeline (Woźniak 2000).

The difference imaging is used for varying luminosity objects and thus this method is suitable to search for gravitational microlensing in very crowded stellar fields. The basic idea of *Difference Image Analysis* (DIA) is to match an analysed image with the best seeing reference image, for astrometric and photometric purposes. Both images need to be registered in the same reference frame, then the subtraction of one from the other can be done which yields the differential flux. This is achieved using a transformation function to determine a convolution kernel that describes the changes in the point-spread function (PSF) between images. The Alard & Lupton (1998) algorithm was designed to derive the convolution kernel as a linear combination of basis functions.

For the data reduction and photometry, we have used PySIS2.4 designed by Michael Albrow for PLANET collaboration (Albrow et al. 2009, submitted). This pipeline is the DIA package with the associated ISIS software.

Before the start of our data reduction process we performed a preliminary image quality review. This one enabled to remove images showing a significant gradient across the field, due to strong background moonlight. Under-exposed images were also removed during this process. In the data reduction process we checked for every data set if reference frame does not contain any image with a bad seeing as well as we rejected entirely saturated images. Furthermore during the review, the images which had a gradient in their sky background due to lack of flat-fielding as well as the saturated ones were removed. Most likely they were affected by the moon during the time of observations. We have decided to exclude one data set because of too short exposure time for the almost half total number of observational points. Such case provides unbelievable values of seeing and a signal to noise ratio. The image quality of two data sets (from Farm Cove and Boyden) for the OGLE 2004-BLG-482 event is poor thus we decided to do not use in our flux measurements and modelling.

3.3.1 Method of Photometry

In the data reduction and photometric measurements process, several important parameters were taken into account: the signal-to-noise ratio (S/N) which indicates how strong and clear is the flux from given object on an image, the gain of the detector, the pixel scale, the saturation level (in Analog-to-Digital Units ADU) which is the ratio between the full well capacity (in e^-) and the full-width at half-maximum (FWHM) of a Gaussian profile. The list of the used telescopes and data reduction parameters is shown in Table 3.1.

The process of DIA starts with the choice of a reference image (a template). Using PySIS, the first step of the data reduction process is to register the images for the subtraction from a reference frame. For the registration of images an astrometric reference image needs to be chosen. In most cases it is a single image with the best (the lowest) seeing. However the lowest seeing can be due to the relative too short exposure time. Then the signal-to-noise ratio is not sufficient.

In the stage of registration each image is transformed geometrically with the astrometric reference image and registered in the coordinates of the astrometric template taking into account the number of stars.

Usually it is a single image characterised by a good seeing and a low background. In the PySIS pipeline the reference frame is created by the stacking of several images. The criteria of choice for the reference frame images are: the seeing, background and ellipticity. The template being the combination of a few good images provides a higher signal-to-noise ratio and lower

background. Moreover this way allows to remove eventual cosmic-rays. Therefore this option is used if possible than a single image. The process of the reference images choice by the pipeline PySIS is automatic. However, it is worthwhile to check the images quality which were taken in particular according to the values of seeing and background.

In the next step, a target is identified from the OGLE finding image which corresponds to a given microlensing event and a measurement of flux on a target is done. The total flux $F(t)$ of target detected by k -th telescope is given by

$$F^{(k)}(t) = A(t) \times F_S^{(k)} + F_B^{(k)}, \quad (3.1)$$

where a source flux F_S and background light F_B are measured in k -th site/detector, and the magnification $A(t)$ is the common quantity for all monitoring telescopes.

Each scaled image is subtracted from the reference frame. The image subtraction process is controlled in PySIS by a scale factor. Its value should be ~ 1.0 in the case of a well-subtracted image taking into account the exposure time of a given image. In general, for the same reference frame and a given image exposure time, a higher value (> 1.0) can indicate that the reference frame is not bright enough or the astrometric frame is incorrect. Whereas a scale factor smaller than 1 tells us about some variations due to small clouds during a given exposure.

In the last step the results of photometric measurements are saved in .pysis and .report files. Moreover the photometric results obtained by the PySIS may be checked with a few diagnostic output files: a mosaic stamp picture of the subtracted images.

Table 3.1: Data reduction parameters for the OGLE 2004-BLG-482 microlensing event

Telescope	Detector	Filter	Pixel scale ["/pixel]	Saturation [ADU]
Danish 1.54m	DFOSC EEV 2K×4K	R	0.390	60×10^3
Canopus (UTas) 1.0m	SITe 512×512	I	0.434	60×10^3
Perth-Lowell 0.6m	Apogee AP7 CCD	I	0.600	50×10^3
CTIO-Yale 1.0m	Apogee AP7B	I	0.469	59×10^3
Auckland 0.35m	Apogee Ap8p SITe003	clear	1.000	30×10^3
Palomar 60inch	SITe 2K × 2K	I	0.378	50×10^3
CTIO 1.3m	ANDICAM	I	0.369	55×10^3
Wise 1.0m	Tektronix 1K	I	0.700	28×10^3
Farm Cove 0.35m	ST-8XME SBIG	clear	1.460	35×10^3

3.3.2 Data Fitting and Minimisation Methods

To derive the microlensing parameters of a given model we have to fit a theoretical light curve to the data sets. In order to estimate the maximum likelihood of a model, thus the goodness of the fit, we find the set of b_1, \dots, b_M model parameters for which the chi-square function χ^2 given by

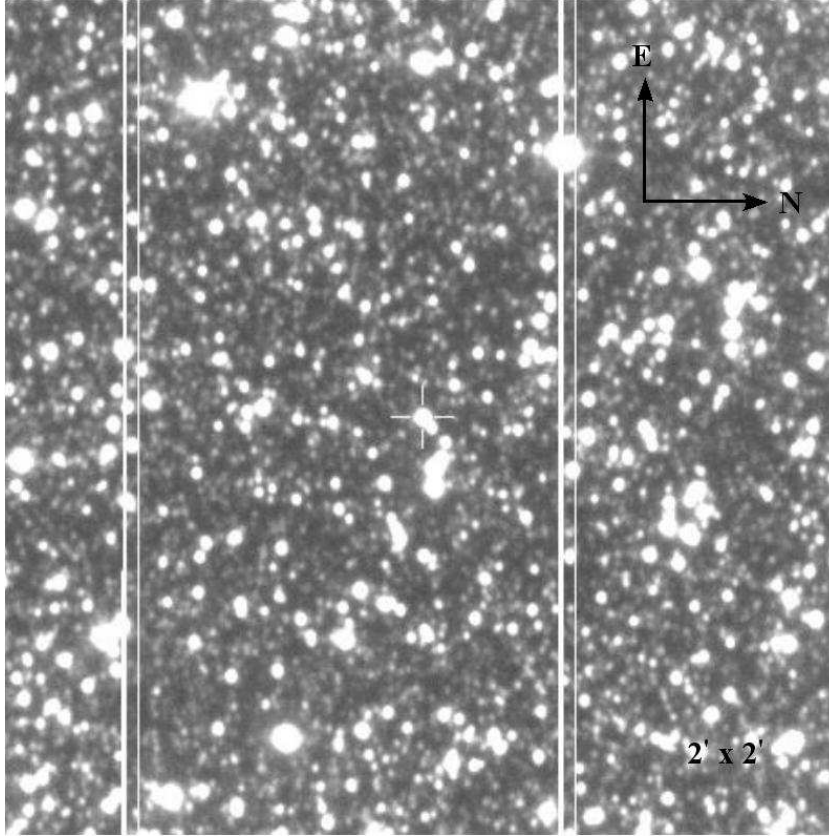


Figure 3.3: Finding chart of the OGLE 2004-BLG-482 microlensing event. The frame scale is $2' \times 2'$ and the field of view has a North-right and East-up orientation. The target position is indicated by an open red circle at the centre of the cross. (credit: EWS web page of OGLE, <http://ogle.astrouw.edu.pl/ogle3/ews/2004/ews.html>)

$$\chi^2 = \sum_{i=1}^N \left(\frac{y_{\text{obs},i} - y_{\text{model}}(x_i; b_1 \dots b_M)}{\sigma_i} \right)^2 \quad (3.2)$$

reaches its minimum value. In Eq. (3.2) N denotes the number of data for which the best-fit model is searched, $y_{\text{obs},i}$ is an observed data point with the uncertainty σ_i at i -th time and y_{model} is a value from the model of b_1, \dots, b_M parameters.

The reduced $\chi^2/\text{d.o.f.}$ (d.o.f. the degrees of freedom) can be expressed as

$$\chi^2/\text{d.o.f.} = \frac{1}{N - N_p} \sum_{i=1}^N \left(\frac{y_{\text{obs},i} - y_{\text{model}}(x_i; b_1 \dots b_M)}{\sigma_i} \right)^2, \quad (3.3)$$

where N_p is the number of fitting parameters. The goodness of fit for a given model is suitable if the $\chi^2/\text{d.o.f.}$ value is around ~ 1 . To minimise the χ^2 function, many approaches can be used, *i.e.* such as Powell's algorithm, Simplex method (e.g. described by Press et al. (1992)), genetic algorithm or Markov Chain Monte Carlo.

3.4 Red Clump Giants Method

The measurement of distances to astronomical objects is one of the most important and difficult questions in astronomy. There are a few methods to achieve it. A good candidate for a distance indicator should be a standard candle abundant enough to provide many examples within reach of parallax measurements. Also, they have to be sufficiently bright to be detectable out to the local group galaxies. As demonstrated by Paczyński & Stanek (1998), the *Red Clump Giants* (RCG) are a good tool to determine astronomical distances. They found empirically that the average absolute magnitude of the red clump stars as measured in the Cousins's *I* band is independent on their (V-I) colour. The value of the RCGs mean absolute magnitude was determined by Stanek & Garnavich (1998) using Hipparcos data. This quantity $M_{I,RC} = -0.23 \pm 0.03$, was recently confirmed by Groenewegen (2008) with $M_{I,RC} = -0.22 \pm 0.03$. The stars of a red clump are metal rich equivalent of the horizontal branch giants. From theoretical models, one expects that their absolute magnitudes weakly depends on their chemical compositions, age and initial stellar mass.

We used in particular this method to estimate the distance to the source star of the Galactic OGLE 2004-BLG-482 microlensing event (Sec. 5.5).

I have participated in a similar data reduction process and analysis of photometric data as well as in observations of the OGLE 2007-BLG-472 microlensing event (Kains et al. 2009).

Chapter 4

Planet Detection through Microlensing

The point-lens point-source case described in Sec. 2.5 is the most simple amongst possible microlensing events. The most common anomalous microlensing events – around 10 percent of all microlensing events – are caused by binary lenses. The binary lenses also describe well planetary systems acting as microlenses. In this chapter we present the results of modelling and analysis of six high magnification events. Two among them are of great interest due to the search for extrasolar planets and four ones show the possibility to study the planet detection efficiency.

4.1 Planetary Microlensing

A planetary system can be discovered if it acts as a microlens of a Galactic bulge background star. The detection of extrasolar planets by microlensing is possible because the presence of planet can be detected through a perturbation in the single lens light curve (Mao & Paczyński 1991; Gould & Loeb 1992). The prediction to discover a terrestrial planet by microlensing came true with the discovery of OGLE 2005-BLG-390Lb (Beaulieu et al. 2006). The possible properties of this $5.5 M_{\oplus}$ cold “Super-Earth” exoplanet were considered by Ehrenreich et al. (2006). Another important event allowed to detect a Jupiter/Saturn analog planetary system in OGLE 2006-BLG-109Lb,c (Gaudi et al. 2008). It provided for the first case a planetary system found by microlensing in which there are constraints on the planetary orbital parameters besides the projected separation onto the plane of the sky.

The time scale of single lens light curve deviations due to the presence of the planet can be of the order of days for giant planets and hours in the case of terrestrial ones. This effect can be used to detect a planetary signal for the range of planet masses from those of gas giants to Earth-like planets (Bennett & Rhie 1996). Assuming the presence of a planet, the detection probabilities range from tens of percent for Jovian planets to a few percent for terrestrial planets (Gould & Loeb 1992; Bennett & Rhie 1996).

The presence of a planet affects the light curve by two parameters, which are the planet-to-star mass ratio $q = \frac{m_p}{m_*}$, where m_p denotes the planetary mass and m_* is the mass of its host star and their separation parameter, d projected onto the lens plane, in Einstein ring radius units θ_E . To yield a detectable deviation, a planet has to take place near one of the two images. Furthermore these images are always close to the Einstein ring when the source is magnified. The sensitivity of the microlensing technique depends on the planet-star separation and peaks

for the separation of 0.6 to 1.6 θ_E , the so-called “lensing zone”.

There are two different scenarios by which planetary systems can be detected through microlensing. One of them happens when a background source star crosses a planetary caustic. In the planetary lensing case, binary lenses (planet + host star) create extended caustics (a central caustic and a larger planetary caustic). The total area enclosed by these curves in comparison with the surface of the Einstein ring disk is very small. However, if the source approaches sufficiently close to or crosses the planetary caustic it can reveal its presence by a signature in the light curve. In general, this effect occurs at lower magnifications. In this kind of planetary microlensing events it is possible to obtain the more accurate planetary parameters. This kind of perturbations cannot be predicted therefore dense and continuous sampling is necessary for microlensing observations. Moreover the planet detection probability per event is low thus the monitoring of many events must be performed. The other channel where microlensing technique can detect planets is by monitoring of high magnification events. We concentrate on this kind of events in the following.

4.2 High Magnification Events

A point-like lens high magnification event occurs when a lens crosses a source star very close to the line of sight, *i.e.* the distance of closest approach is much smaller than the Einstein ring radius: $u_{\min} \ll 1$, where u_{\min} is expressed in units of θ_E . Close to the light curve peak of high magnification events, two elongated individual source images then sweep along the Einstein ring. In the case of a binary lens, a planetary companion to its host star near the Einstein ring will distort the symmetry of the ring. In the source plane high magnification events can be explained as those caused by the source star approaching the central caustic. In these events the maximum magnification reads $A_{\max} \simeq 1/u_{\min} \gg 1$.

For very high magnification events (as $A \gtrsim 100$), nearly the entire Einstein ring radius is probed. This fact makes the high magnification events particularly sensitive to the presence of planet. Moreover, this effect does not depend on the planet orientation with respect to the source trajectory. Thus the high magnification events provide great opportunities to detect existing planets close to the Einstein ring radius and sensitive to low-mass planets (Griest & Safizadeh 1998). Although high magnification events are infrequent (in the 2008 PLANET observing season this sort of event is about 20 percent of all observed microlensing events) it is possible to predict them several hours to several days before their peak appears. Furthermore the time interval of high sensitivity to the planetary signal is predictable from the evolution of the light curve (Griest & Safizadeh 1998). It happens within a full-width half-maximum of the event peak or typically around a day for these events (Rattenbury et al. 2002).

High magnification events are limited by extended source effects (like example for a giant $\sim 10R_{\odot}$. In the case of a main-sequence star (around $1R_{\odot}$) as a source the central caustic can be probe. For the cool, Jovian-mass planet involved in the high magnification event, MOA-2007-BLG-400Lb (Dong et al. 2008), the angular extent of the region of perturbation due to the planet is significantly smaller than the angular size of the source. Therefore the planetary signature is also smoothed out by the finite source size. The case of a large source size provides the higher probability to detect a planet but its signal is much more hidden in the source flux. With smaller source sizes, although a stronger planetary signal can be observed, the probability of caustic crossing is much less. The OGLE 2005-BLG-169 (Gould et al. 2006) provided the

detection of a Neptune mass ratio ($q \simeq 8 \times 10^{-5}$) planetary companion to the lens star in the extremely high magnification ($A_{\max} \sim 800$) microlensing event. The analysis of this event has shown the utility of high magnification events for the detection of low-mass planets.

We model and analyse such kind of microlensing events to find a planetary signal. High quality data with good data reduction therefore are important as well as a detailed modelling and analysis to increase the chance to detect a planet. Moreover, accurate, well-sampled light curves around the event peaks are necessary. In the case we do not detect a planet, then still high magnification events give us the possibilities to determine limits on the planet presence because of their high sensitivity.

In sections 4.4 and 4.5 we present the modelling and the results of analysis for two high magnification events OGLE 2006-BLG-245 and MOA 2006-BLG-099 which were primary targets to search for extrasolar planets.

4.3 Analysis of 2006 High Magnification Events

4.3.1 Selection of 2006 High Magnification Events

During the 2006 observing campaign, OGLE discovered about 550 microlensing events. We have been working on the modelling and selection of interesting high magnification events during this PLANET observing season.

In first step of the selection, we took into account the following criteria of the choice: a maximum magnification $A \gtrsim 40$, a good coverage of a light curve and the quality of data. According to these criteria we have selected eight OGLE and one MOA events, which are listed in Table 4.1. In the second step we have performed the modelling of six of them using a point-source point-lens (PSPL) model. After this we have obtained four potentially interesting events for different reason (to study other microlensing effects, e.g. extended source effects) and two events of great interest: OGLE 2006-BLG-245 and MOA 2006-BLG-099. These high magnification events could involve a planetary signal. For them in the next step, we have performed the modelling using the point-source binary-lens (PSBL) model.

Table 4.1: The selected 2006 high magnification microlensing events with their sky coordinates, maximum magnifications A_{\max} and baseline magnitudes in the I -band.

Event	R.A. (J2000.0)	Dec (J2000.0)	A_{\max}	I
OGLE 2006-BLG-221	18 ^h 04 ^m 41 ^s .47	−29°43′20″.0	101.2	19.7
OGLE 2006-BLG-229	18 ^h 00 ^m 16 ^s .24	−30°24′12″.6	40.5	18.6
OGLE 2006-BLG-245	18 ^h 02 ^m 36 ^s .47	−29°23′45″.4	195.9	18.4
OGLE 2006-BLG-265	18 ^h 07 ^m 18 ^s .88	−27°47′42″.7	254.6	19.4
OGLE 2006-BLG-416	18 ^h 10 ^m 16 ^s .45	−27°57′15″.4	51.6	17.4
OGLE 2006-BLG-437	17 ^h 57 ^m 47 ^s .65	−29°50′46″.7	225.6	19.4
OGLE 2006-BLG-440	18 ^h 02 ^m 26 ^s .59	−28°50′19″.1	48.2	19.0
OGLE 2006-BLG-451	17 ^h 59 ^m 29 ^s .02	−28°37′18″.4	65.5	18.6
MOA 2006-BLG-099	17 ^h 56 ^m 14 ^s .91	−29°36′54″.2	868.0	21.9

A rather dense sampling of the selected light curves was achieved. We point out that the raw photometry errors obtained from the data reduction process of crowded fields clearly underestimate the true errors (e.g. Woźniak (2000)).

In general, a lensing host star with a planet is modelled by a binary lens with an extreme mass ratio, *i.e.* $q < 10^{-2}$. For each light curve χ^2 was computed using the point-source point-lens (PSPL) model. The detected deviation in a light curve was considered to be due to planetary companion to the host star if the difference between χ^2 values of both models is $\Delta\chi^2 = \chi^2_{\text{PSPL}} - \chi^2_{\text{PSBL}} \geq 60$. We have put this value as a threshold because we have found robust enough to avoid a false detection due to statistical fluctuations and unrecognised systematic errors. This value is also consistent with studies of detection efficiency of microlensing data to planetary companions (Gaudi & Sackett 2000). The PSPL modelling analysis led us to the two microlensing events of great interest: OGLE 2006-BLG-245 and MOA 2006-BLG-099. The high magnification events of less interest are shown and briefly described in Sec. 4.3.2. The two events of main interest are presented and analysed in Sec. 4.4.

4.3.2 PSPL models of 2006 High Magnification Events

We present the point source point lens (PSPL) modelling for these events which we have performed using the GOBI code written by Arnaud Cassan.

A primary lens with an orbiting companion is described by the formalism of binary lenses. The flux still satisfies Eq. (2.20), but the magnification can no longer be calculated analytically. Instead, the lens equation describing the mapping from the source plane (ξ, η) to the lens plane (x, y) must be solved numerically. Following the formalism provided by Witt (1990), the binary lens equation is expressed with the complex notation

$$\zeta = z - \frac{1}{1+q} \left(\frac{1}{\bar{z}} + \frac{q}{\bar{z}+d} \right), \quad (4.1)$$

where $\zeta = \xi + i\eta$ relates to a source and $z = x + iy$ to a lens positions. The coordinate system is chosen so that the more massive component of the binary lens is located at the origin, with the secondary object located on the left at a distance d . This separation between the two lens components is the projected length onto the plane of the sky, in θ_E units and $q \leq 1$ denotes the binary lens mass ratio.

The challenge of microlensing modelling is related to the fact that the binary lens magnification cannot be expressed in a closed analytical form and its multi-dimensional parameter space has a complicated χ^2 -surface.

OGLE 2006-BLG-265

The light curve of the OGLE 2006-BLG-265 microlensing event is shown in Fig. 4.1. It has a good coverage of the peak region with PLANET and MOA data sets, as well as the wings with PLANET data. The MicroFUN (p - Palomar) observational points located in the central part of the curve do not show any trend. On the right wing of the curve there is an apparent trend of MicroFUN (c-CTIO) data which is not consistent with OGLE (O) and Danish (Z) observational points. There is some trend for the data MicroFUN (c) but also there is clear correlation of those data with their background data. There is a data problem with the Boyden telescope (high residual in sigma for a lot of data). The new data reduction is needed for the SAAO (A) and UTas (U) data sets. The error bars are underestimated for the PLANET data (A and U, they are

very small). The ESPL model is not a proper model for this event (a source radius $< 10^{-2}$). The maximum magnification of this event reached the value $A_{\max} \approx 210$. The range of time for this high magnification is very short. In this case an extended source size effect is rather not observed. I have performed the modelling for this event using the extended-source point-lens (ESPL) and PSPL models. Both models are comparable in the term of fit goodness expressed by χ^2 for the same number of degree of freedom. Maybe would be nice to use MOA data to check. This event could be worth to be used in search of planetary signal detection efficiency after the data re-reduction.

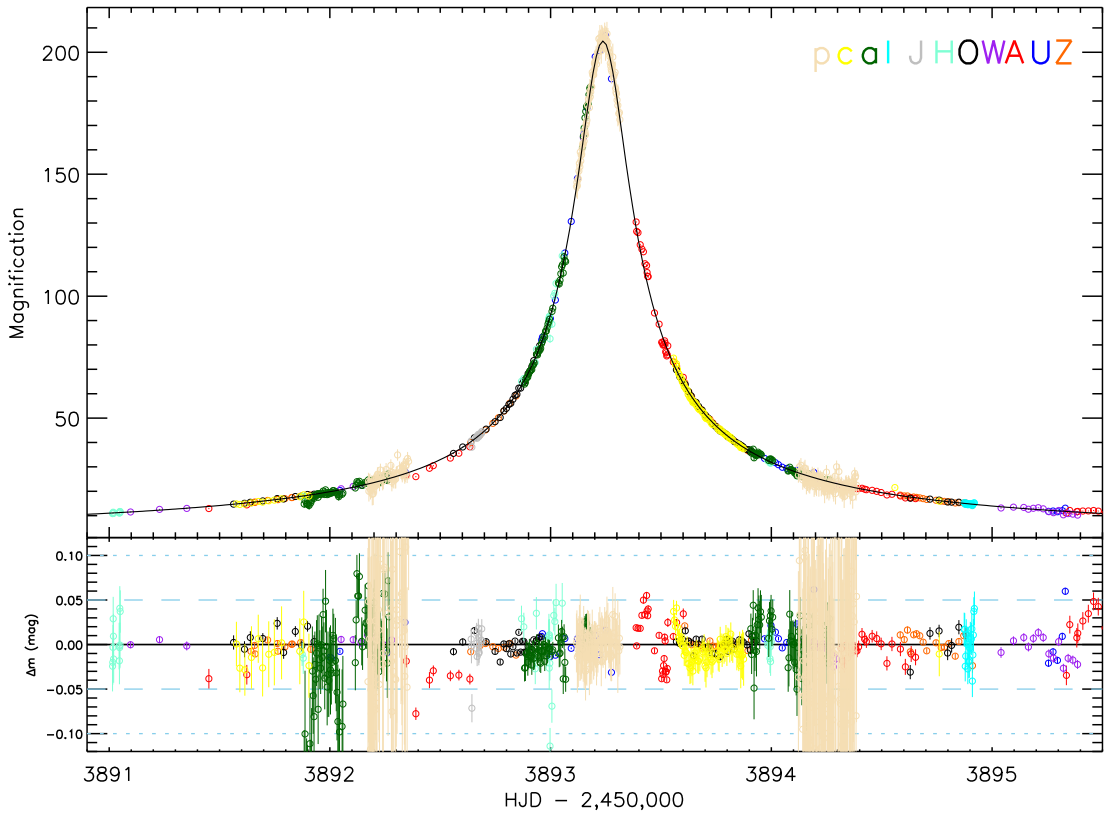


Figure 4.1: Light curve of OGLE 2006-BLG-265 microlensing event using the point-source point-lens model and PLANET (W, A, U, Z), MicroFUN (p, c, a, l), OGLE (O) and RoboNet (J, H) data sets. In the lower panel the residuals in magnitudes are displayed.

OGLE 2006-BLG-416

For the OGLE 2006-BLG-416 event we note a good coverage of the central part of its light curve with PLANET/RoboNet, MicroFUN and OGLE data and the wings with PLANET and OGLE data (Fig. 4.2). Its photometric measurements were performed in the *I*-band except RoboNet (J) data set which was measured in the *R*-filter. The UTas (U) observational points

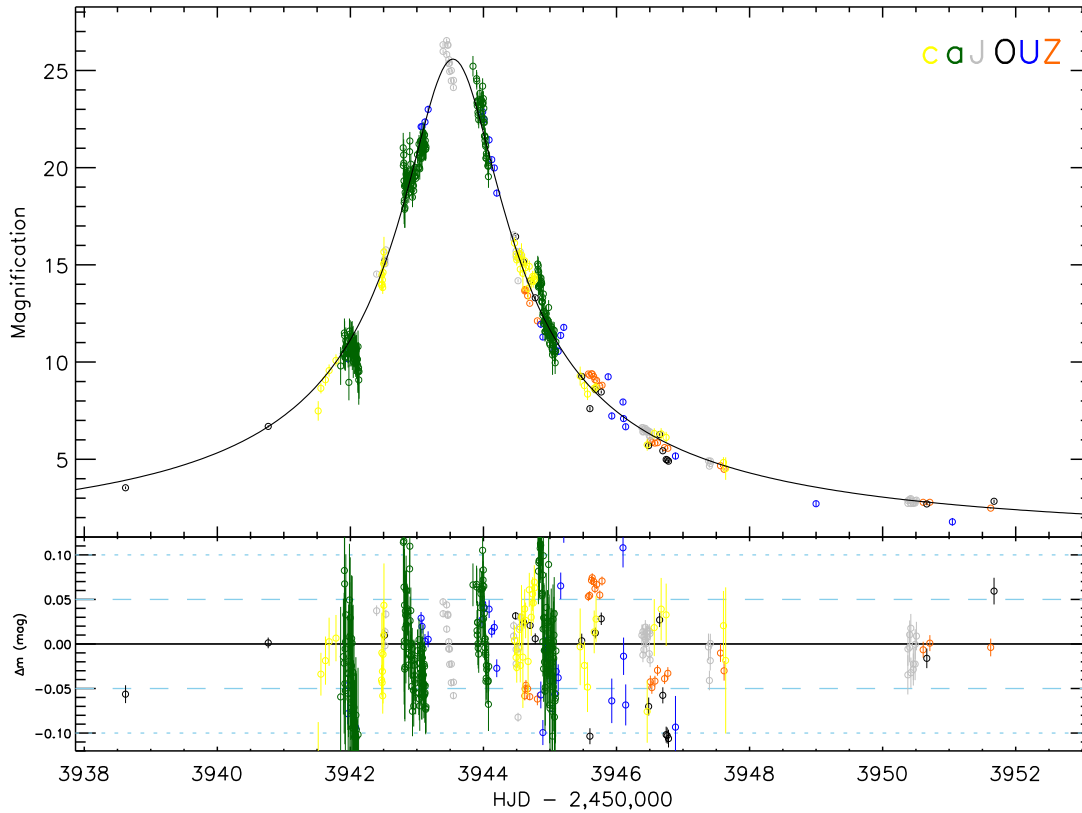


Figure 4.2: The point-source point-lens fit of OGLE 2006-BLG-416 microlensing event with PLANET (U, Z), MicroFUN (c, a), OGLE (O) and RoboNet (J) observational data. In the lower panel the residuals in magnitudes are displayed.

show some scatter on the right wing of the curve, some of them might indicate an anomaly. The baseline for the UTas (U) data set is not very well determined. The OGLE (O) and Danish (Z) points show a similar trend but they are not consistent. In the peak region of the light curve, $t = (3943 - 3944.5)$ UTas (U) and MicroFUN (a-Auckland) data are consistent. There is a problem of Boyden observational data (high residual in sigma for many data) therefore we decided to exclude this set from the modelling. We also note the error bars for (f) Farm Cove data (MicroFUN) are too large. The ESPL model is comparable to PSPL one and it is not a proper model for this event. The Einstein time for this high magnification is short. We find that there are not extended source size effects in this case (a source radius around 10^{-2}). This event with the good coverage at the peak remains interesting for detection efficiency estimation. However, a new data reduction would be necessary.

OGLE 2006-BLG-229

The photometry of the OGLE 2006-BLG-229 event is displayed in Fig. 4.3. In general, its light

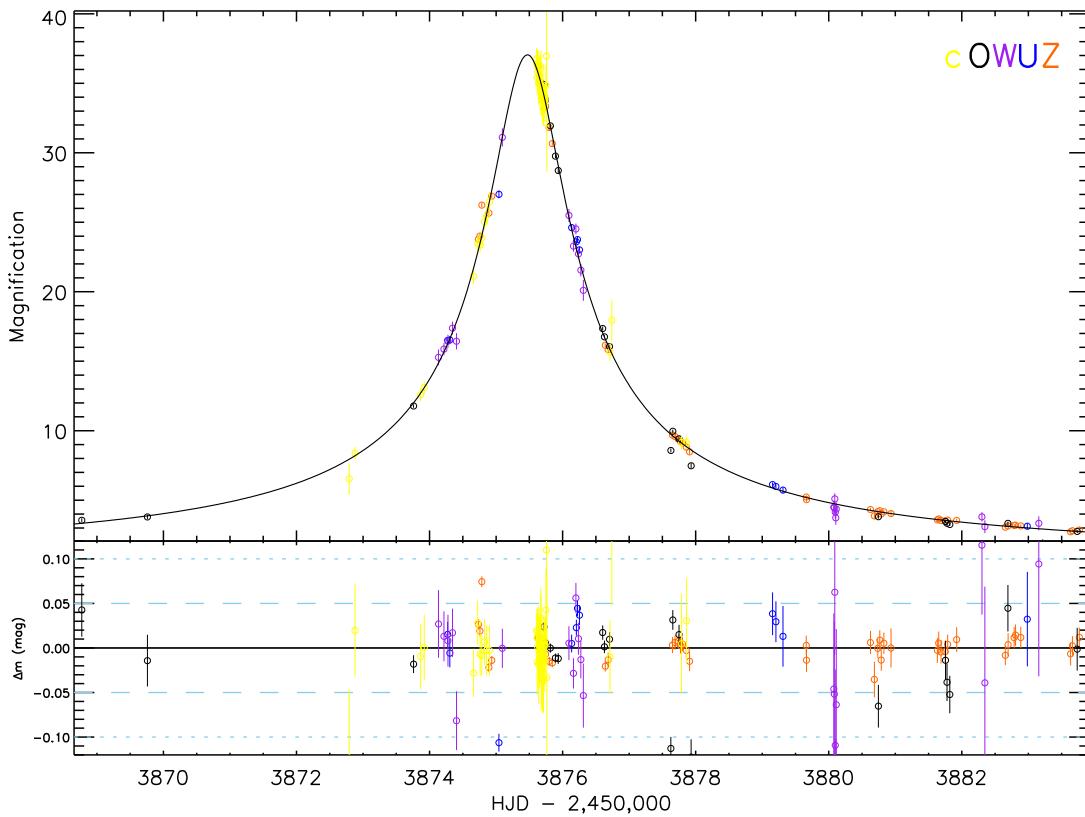


Figure 4.3: Point-source point-lens light curve of OGLE 2006-BLG-229 microlensing event fitted PLANET (W, U, Z), MicroFUN (c) and OGLE (O) data sets. In the lower panel the residuals in magnitudes are displayed.

curve is not well-defined by the observational data. The peak region of the light curve is not covered enough. The data points are consistent only for small part of the curve. We had to remove during the modelling the Boyden data set. The observational points from that set were scattered. For this event it is difficult to determine a trend in the residuals for the peak region of this light curve.

OGLE 2006-BLG-440

The point-source point-lens fit of the OGLE 2006-BLG-440 data is displayed in Fig. 4.4. In the case of this event the wings of the light curve are not very well-defined for the OGLE (O) data set. The UTas (U) and Boyden (F) observational data are scattered. In the peak region of the curve the data points are consistent only for a small part. The central part of the light curve is not covered enough.

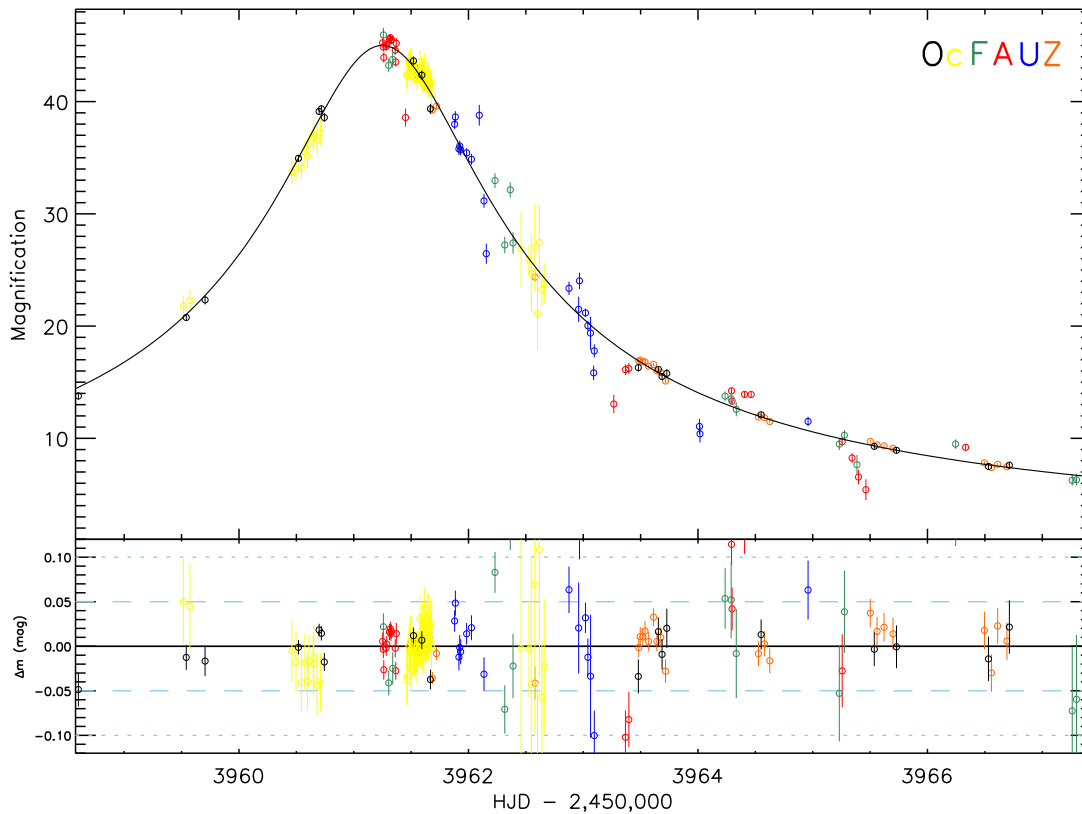


Figure 4.4: Magnification curve of OGLE 2006-BLG-440 microlensing event for PLANET (F, A, U, Z), MicroFUN (c) and OGLE (O) data sets. In the lower panel the residuals in magnitudes are displayed.

Rejected events

The OGLE 2006-BLG-437 event has a good coverage of the peak region of its light curve by MOA and OGLE data. However, the PLANET data (Danish, Boyden, SAAO) on the right wing of its curve are not consistent with each other and some of them are scattered. Moreover, there are two big gaps in PLANET data on the right wing of the light curve. The OGLE 2006-BLG-451 light curve has a relatively good coverage of its central part by PLANET, MOA and OGLE observational data. However, there are a few gaps of data. For OGLE 2006-BLG-221 event we

noted a few gaps in the coverage of its light curve. The OGLE data on the wings of this curve are scattered. A bad coverage of the central part of the light curve. In the case of OGLE 2006-BLG-195, we pointed out a bad coverage of the central part of the light curve. Also, there are a few gaps of data. The OGLE data are scattered on the wings of the curve. In general, the light curve of this event is not well-defined by data points.

4.4 Modelling of OGLE 2006-BLG-245

In this section we present the results of modelling and analysis of OGLE 2006-BLG-245. From the data online models there was the suspicion of a planetary companion signal. This bulge microlensing event was detected and alerted by the OGLE collaboration (Udalski 2003) on 2006 ($\alpha = 18^{\text{h}}02^{\text{m}}36.47^{\text{s}}$, $\delta = -29^{\circ}23'45''.4$ (epoch J2000.0)). Its observed brightness at baseline was $I_{\text{OGLE}} = 18.432 \pm 0.002$. The photometric monitoring observations of OGLE 2006-BLG-245 event were performed by OGLE, MOA, five PLANET telescopes, six MicroFUN in the I band and by two telescopes belonging to the RoboNet collaboration in R filter.

Some amount of data have been excluded due to the high value of seeing (MicroFUN MDM (m), RoboNet (H)) and error mag (MOA (K)) and some of them are scattered unreasonable (SAAO (A), Boyden (F)). Our final data set consists of 464 points from OGLE, 346 data from the five PLANET telescopes Danish 1.54m, UTas, Perth, SAAO and Boyden, 798 points from MOA, 766 data from the six μ FUN observational sites Auckland, MDM, CTIO, Wise, Palomar and LOAO, and 100 data from two 2.0m robotic telescopes of RoboNet team (the Faulkes North telescope in Hawaii and the Faulkes South one in Australia) which amounts to a total of 2474 measurements. The photometric data sets used in the modelling and analysis are presented in Table 4.2.

Figure 4.5 presents the resulting light curve of OGLE 2006-BLG-245 microlensing event. The time scale at the abscissa is given as Modified Heliocentric Julian Date, $\text{MHJD} = \text{HJD} - 2,450,000$. In the Fig. 4.6 is displayed the central part of light curve. We could note that the MOA (K) and UTas (U) observational data in the peak region are not consistent.

The fits of the point-source point-lens (PSPL) and the point-source binary-lens (PSBL) models of the OGLE 2006-BLG-245 event we obtained using a code – *GOBI* written by Arnaud Cassan. The PSPL and PSBL modelling we performed for the same sampling of data set. The best fit PSPL and PSBL model parameters are presented in Table 4.3.

As a result, we find that the observed features of the light curve cannot be reproduced using a binary microlensing model with an extreme (planetary) mass ratio. The fit using a point-source binary-lens (PSBL) model is slightly better than PSPL fit but the difference of total $\Delta\chi^2$ between PSBL fit and PSPL fit $\Delta\chi^2 = \chi^2_{\text{PSBL}} - \chi^2_{\text{PSPL}} = -9.841$ is not really significant. In this case it appears that the planetary model does not differ significantly from the point source point lens model. We conclude that finally there is no evidence for a planetary signal in this event.

Table 4.2: The summary of OGLE 2006-BLG-245 data sets – the number of data points and the name for every used site. The third column shows the χ^2 values per data set for the final PSPL model.

Telescope	Data	χ^2
Z ... Danish	141	81.8
U ... UTas	101	187.8
W ... Perth	44	71.3
A ... SAAO	36	288.5
F ... Boyden	24	49.3
O ... OGLE	464	456.5
K ... MOA	798	538.9
a ... Auckland	87	44.5
m ... MDM	141	505.7
c ... CTIO	106	97.3
w ... Wise	116	62.0
p ... Palomar	31	279.6
l ... LOAO	285	151.2
H ... Faulkes T. North	41	5.5
J ... Faulkes T. South	59	82.1

Table 4.3: Parameters of our best-fit to the OGLE 2006-BLG-245 data obtained by OGLE, PLANET and MicroFUN for the point-source point-lens (PSPL) and the point-source binary-lens (PSBL) models . The χ^2 values are based on the rescaled photometric errors.

Parameter	Single lens	Binary lens
q	–	7×10^{-6}
d	–	9.179×10^{-1}
ϕ	–	1.643×10^{-2}
t_E [days]	57.146	55.815
t_0 [days]	3885.055	3885.054
u_0	4.783×10^{-3}	4.898×10^{-3}
$\chi^2/\text{d.o.f.}$	2901.897/2474	2892.056/2474

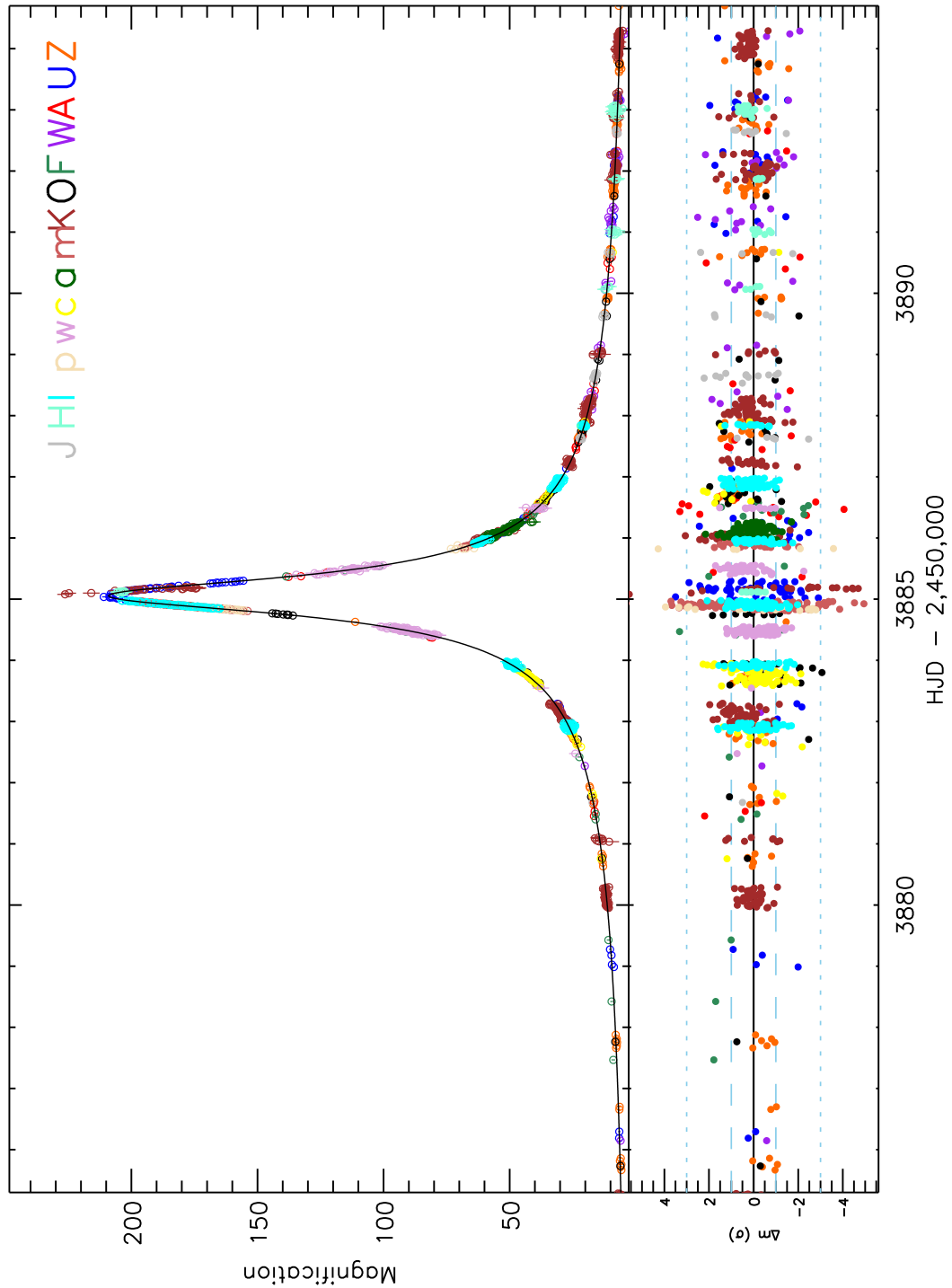


Figure 4.5: Photometry of OGLE 2006-BLG-245 microlensing event. Modelling using the point-source point-lens model. The data points are indicated by a colour of their origin telescope character. PLANET (F, W, A, U, Z), MicroFUN (l, p, w, c, a, m), OGLE (O) and MOA (K) data sets. In the lower panel the residuals in the term of sigma are displayed.

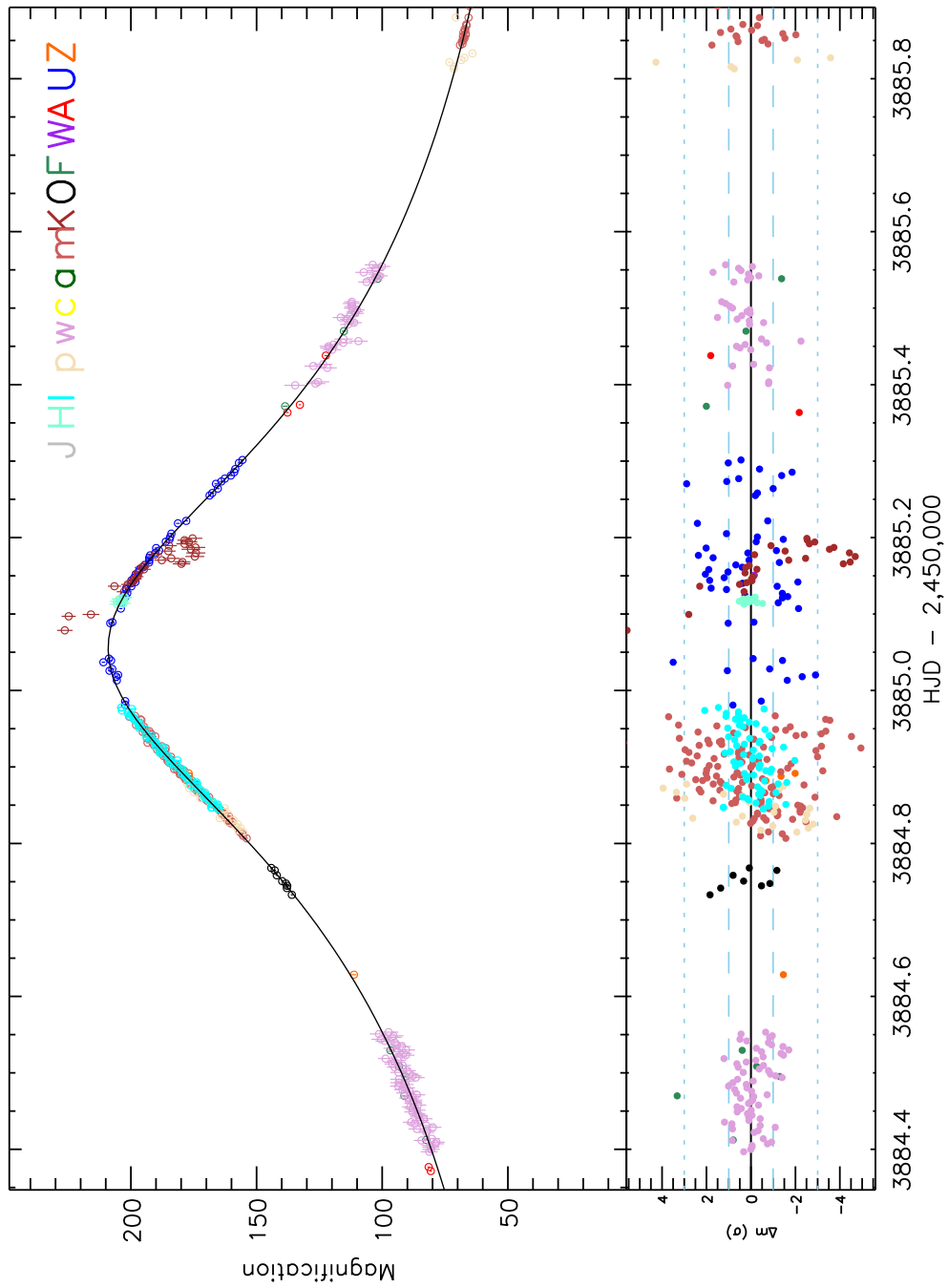


Figure 4.6: The peak region of OGLE 2006-BLG-245 light curve. In the lower panel the residuals in the term of sigma are displayed.

4.5 MOA 2006-BLG-099

Photometric observations performed by MOA, PLANET and MicroFUN teams on the high magnification event MOA 2006-BLG-099 ($A_{\max} \simeq 868$) show a small deviation from the single lens light curve. This perturbation takes place at the peak region. For this event we fitted the photometric data from MOA, OGLE, three observing sites of PLANET: the Danish 1.54 m at ESO La Silla (Chile), the Canopus 1.0 m (UTas) near Hobart (Tasmania), the Rockefeller 1.5 m of the Boyden Observatory at Bloemfontein (South Africa) and four telescopes of MicroFUN: Auckland, CTIO, Farm Cove and LOAO. The data sets used in modelling are shown in Table 4.4.

Table 4.4: Data sets of MOA 2006-BLG-099 used for modelling with the name of site and the number of observational data. The χ^2 values per data set for the best-fit PSPL model are shown in the third column.

Telescope	Data	χ^2
Z ... Danish	68	504.5
U ... UTas	54	148.9
F ... Boyden	64	1721.0
O ... OGLE	115	305.9
K ... MOA	609	2922.0
a ... Auckland	120	119.9
c ... CTIO	19	6.312
f ... Farm Cove	46	17.0
l ... LOAO	54	88.8

As for OGLE 2006-BLG-245, we have performed the modelling using the point-source point-lens (PSPL) and point-source binary-lens (PSBL). PSBL I involved d and q as fixed model parameters and PSBL II model with free parameters. The best corresponding parameter sets are presented in Table 4.5.

The total $\Delta\chi^2$ for PSBL I and PSBL II models are respectively $\Delta\chi_{\text{I}}^2 = \chi_{\text{PSBL I}}^2 - \chi_{\text{PSPL}}^2 = -0.878$ and $\Delta\chi_{\text{II}}^2 = \chi_{\text{PSBL II}}^2 - \chi_{\text{PSPL}}^2 = -1.824$. Both values indicate that the differences between these model parameters and PSPL are not significant enough to state about the planet signal. However, the question of planetary presence in this event should be investigated further through the parameter space. We find that the observed deviation from the point-source point-lens light curve of MOA 2006-BLG-099 is not a planetary signature.

Table 4.5: Parameters of our best-fit to the data obtained by MOA, OGLE, PLANET and MicroFUN for the point-source point-lens (PSPL) and the point-source binary-lens (PSBL) models. The χ^2 values are calculated on the base of photometric errors without rescaling factors.

Parameter	PSPL	PSBL I	PSBL II
q	—	7.0×10^{-6}	1.237×10^{-4}
d	—	8.530×10^{-1}	6.400×10^{-1}
ϕ	—	3.154×10^{-1}	3.738×10^{-1}
t_E [days]	22.971	28.609	28.900
t_0 [days]	3940.349	3940.349	3940.347
u_0	2.517×10^{-3}	2.023×10^{-3}	1.949×10^{-3}
χ^2 /d.o.f.	5834.022 / 1149	4825.475 / 1149	3738.622 / 1149

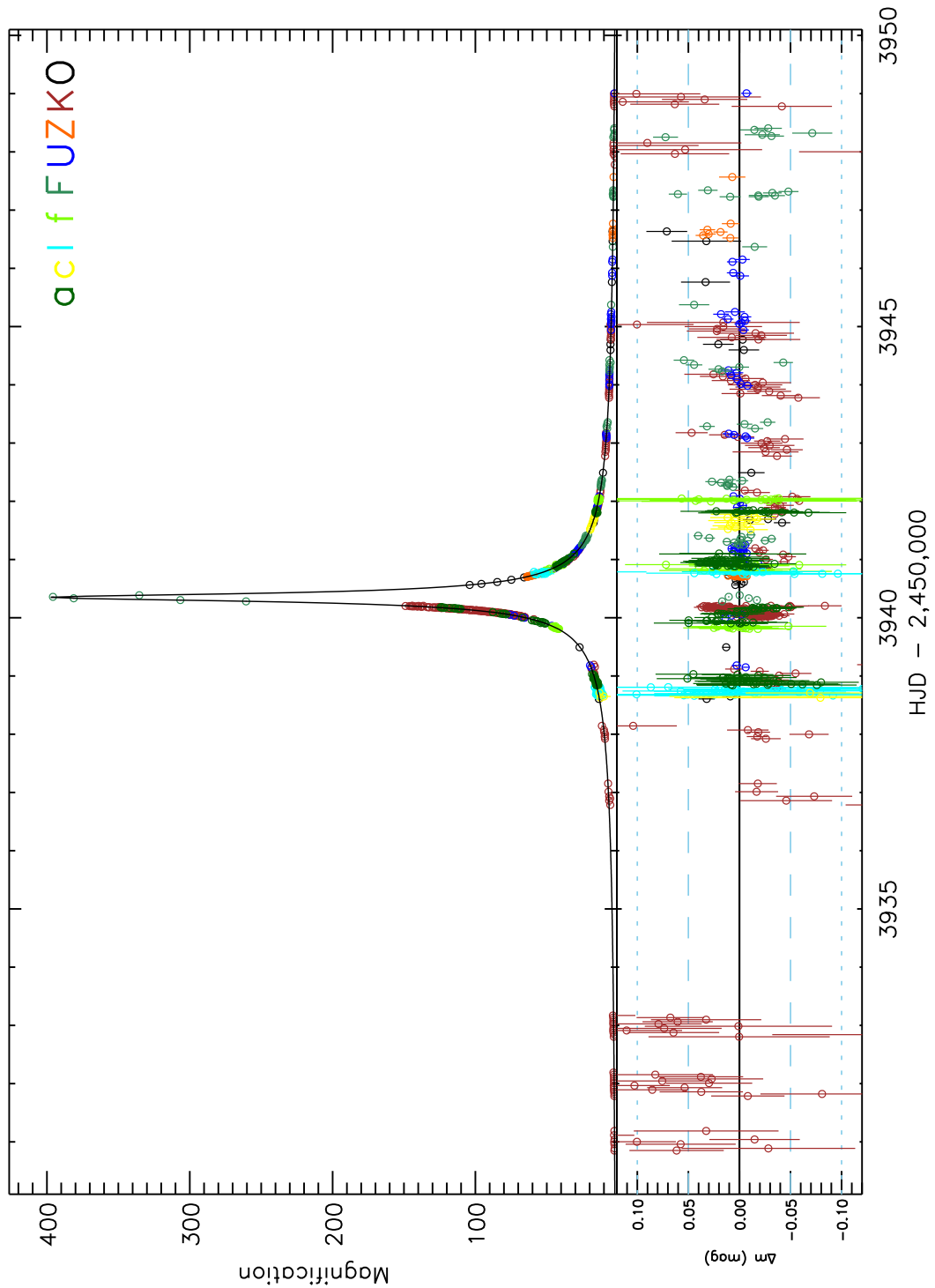


Figure 4.7: Light curve of the MOA 2006-BLG-099 microlensing event with the point-source point-lens model fitted to PLANET (F, U, Z), MicroFUN (a, c, l, f), MOA (K) and OGLE (O) data. The residuals in magnitudes are shown in the lower panel. The observational points are indicated by a colour of their origin telescope character.

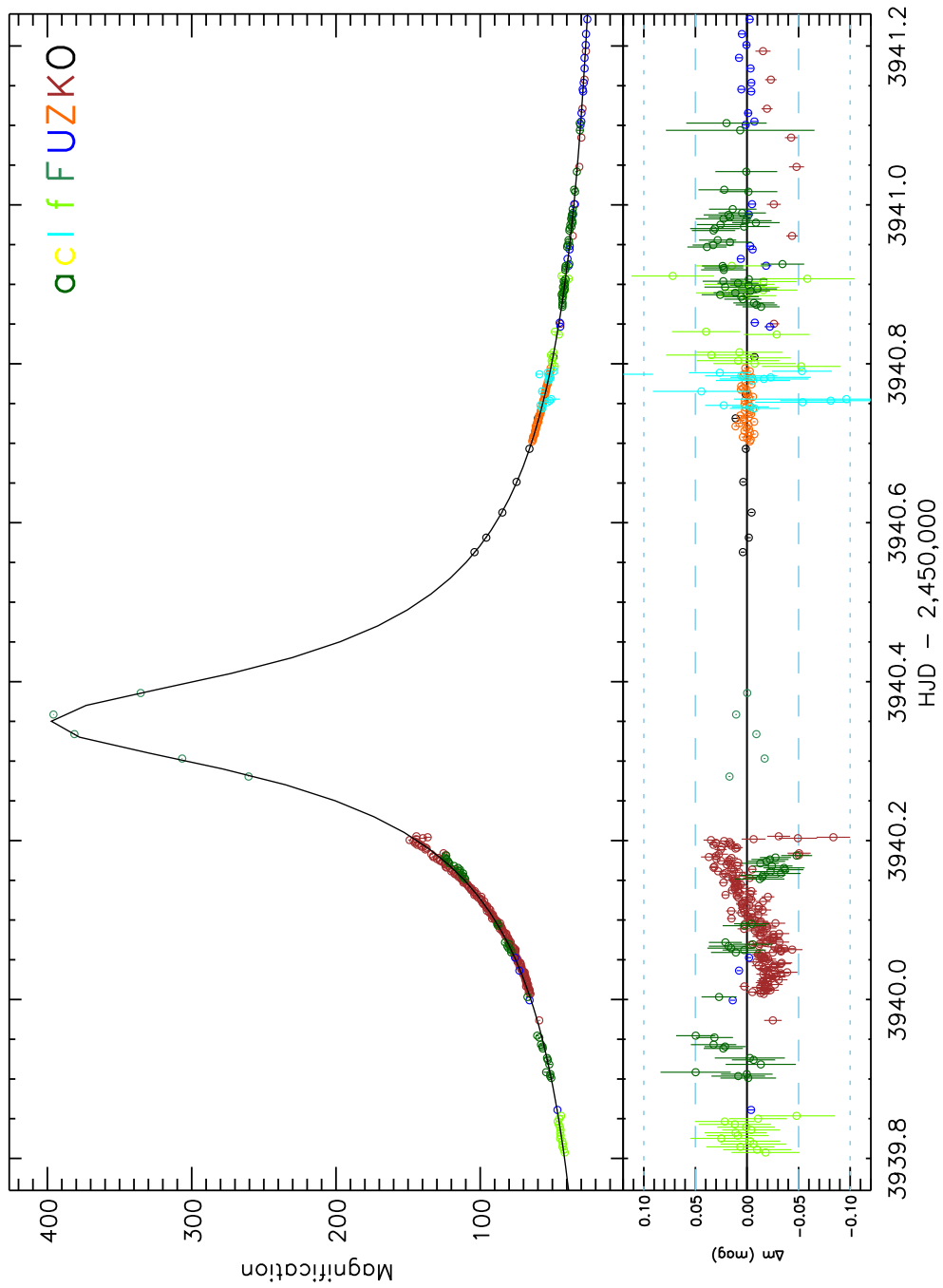


Figure 4.8: The peak region of MOA 2006-BLG-099 light curve with the point-source point-lens model. In the lower panel the residuals in magnitudes are displayed.

4.6 Conclusion on the 2006 High Magnification Events

We have shown with our detailed modelling and analysis that neither the OGLE 2006-BLG-245 nor the MOA 2006-BLG-099 microlensing event involve any planetary deviations. We have performed a careful data reduction of the selected high magnification events from the 2006 observing season. From a comparison between a single lens and a planetary lens model, we have concluded that there is no evidence for any planetary signal in used observational data sets. These high magnification events remain anyway very sensitive to the presence of planets, and they can be used to compute upper limits on the presence of planet which could be a follow-up work of this study.

Chapter 5

A Detailed Study of Extended Source Event: OGLE 2004-BLG-482

In this chapter the Galactic microlensing event OGLE 2004-BLG-482 is presented as the case of event with a finite source effect and limb darkening. In Sec. 5.2 we present the OGLE 2004-BLG-482 event, our photometric data and our data reduction procedures. We perform a detailed modelling of the light curve in Sec. 5.4. The fundamental properties of the target source star are derived in Sec. 5.6. Sec. 5.7 is dedicated to a detailed analysis of the measured linear limb-darkening coefficients and their comparison with model-atmosphere predictions. Finally in Sec. 5.8, we perform a similar analysis using an alternative description of limb darkening based on a principal component analysis of ATLAS limb-darkening profiles.

5.1 Introduction

Photometric observations of stars yield their spectral types and other information useful for studying their atmospheres. However, much of the information on the structure of the atmosphere and related physical processes is lost in the disk-integrated flux. Advanced models calculated for a broad range of stellar types (e.g. MARCS, Gustafsson et al. (2008) ; ATLAS, Kurucz (1992) ; Plez et al. (1992)) describe the corresponding physics at different optical depth, which can potentially result in observational signatures if the star's disk is spatially resolved. In particular, this information is present in the star's limb-darkening profile, which is the variation of intensity from the disk centre to the limb. Only a few observational methods such as stellar interferometry, analyses of eclipsing binaries, transiting extrasolar planets and gravitational microlensing are able to constrain in suitable cases stellar limb-darkening.

A Galactic gravitational microlensing event (Paczynski 1986) occurs when a foreground massive object passes in the vicinity of the line-of-sight to a background star, resulting in a transient brightening of the source star (called magnification, or amplification). Microlenses can spatially resolve a source star thanks to caustic structures created by the lens. They are formed by a single point or by a set of closed curves, along which the point-source magnification is formally infinite, with a steep increase in magnification in their vicinity. In practice, this increase is so steep that the characteristic length scale of the differential magnification effect is on the order of a fraction of the source star's radius. Early works by e.g. Witt (1995) or Loeb & Sasselov (1995) have pointed out the sensitivity of microlensing light curves to limb-

darkening, with the aim to help remove microlensing model degeneracies. The specific use of microlensing as a tool to study stellar atmosphere was proposed later (e.g. Valls-Gabaud 1995; Sasselov 1996; Hendry et al. 1998), in particular to probe Galactic bulge red giant atmospheres (Heyrovský et al. 2000). For a given microlensing configuration, the spatial resolution increases with the source's physical diameter, so that giant stars are primary targets.

Limb darkening measurements by microlensing were performed for a number of main-sequence and giant microlensed stars. Event MACHO 1998-SMC-1 (Albrow et al. 1999a; Afonso et al. 2000) allowed for the first time such a measurement for a metal-poor A6 dwarf located in the Small Magellanic Cloud. Its stellar type was derived from a spectroscopic and photometric analysis in five filters; the lens was a binary star also located in the SMC. No real comparison with atmosphere models could be provided since very little data existed for these metal-poor A stars. The first microlensing limb-darkening measurement for a solar-like star was reported by Abe et al. (2003): the source was identified as an F8-G2 main-sequence turn-off star, involved in the very high-magnification microlensing event MOA 2002-BLG-33 caused by a binary microlens. A good agreement with limb-darkening coefficient predictions was obtained in the *I* band. A limb-darkening measurement for the late G / early K sub-giant was also performed by Albrow et al. (2001) with the binary-lens caustic-crossing event OGLE 1999-BLG-23. The stellar type of the source star was identified by comparing its position on two colour-magnitude diagrams obtained from two different telescopes, and deriving the star's effective temperature from colour calibration. Again, they found a good agreement with stellar models both for the *I* and *R* filters.

Most of the limb-darkening measurements, however, were obtained on Galactic-bulge giant stars. The first case was reported by Alcock et al. (1997) for MACHO 95-30, which involved a very late M4 red giant source star (spectroscopic typing). In this event theoretical limb-darkening coefficients were only used to improve the light-curve fit, but no limb-darkening measurement has been performed. Heyrovský (2003) later argued that the intrinsic variability of the source star precluded any useful limb-darkening analysis. Late M giants are of special interest because they provide an opportunity to test models at the lower end of the temperature range used to compute most of the synthetic model atmosphere grids. For the event MACHO 1997-BLG-28, Albrow et al. (1999b) derived *I* and *V* coefficients for a K2 giant (typing from spectroscopic observations) crossing a caustic cusp and found a good agreement with stellar models predictions. However, in such a complex event, many side effects could have affected the light curve, which somehow decreased the strength of the conclusions. Such a remark holds as well for MACHO 1997-BLG-41 (Albrow et al. 2000), which involved a late G5-8 giant crossing two disjoint caustics.

Microlensing event EROS BLG-2000-5 provided the first very good opportunity to test at high precision limb-darkening of a K3 giant (typing based on both photometry and high resolution spectroscopy) in five filters (Fields et al. 2003). From the comparison of their results to predictions from atmosphere models in the *V*, *I* and *H* filters, they concluded that the discrepancy is unlikely to be due to microlensing light-curve modelling drawbacks, but could rather be explained by inadequate physics in the stellar models that may be not applicable for all surface gravities. A clear variation with time in the shape and equivalent width of the H α line was also reported for the first time in this event (Afonso et al. 2001; Castro et al. 2001). Limb-darkening was also detected in OGLE 2003-BLG-238 (Jiang et al. 2004) and OGLE 2004-BLG-262 (Yoo et al. 2004), which involved early K1-2 giants, but no strong conclusions on limb darkening could be drawn from these events.

From the binary-lens event OGLE 2002-BLG-069 (Cassan et al. 2004; Kubas et al. 2005), it was possible to obtain not only limb-darkening measurements for a G5 bulge giant source star in the I and R bands, but also to test directly, predictions from PHOENIX stellar model atmospheres by comparing the change of the $H\alpha$ equivalent width during a caustic crossing (Cassan et al. 2004; Thurl et al. 2006) using high resolution UVES/VLT spectra. A discrepancy was found between model and observations, which is most probably explained by the lack of a proper chromosphere implementation in the used stellar models. More recently, Cassan et al. (2006) performed limb-darkening measurements for the K3 giant source of OGLE 2004-BLG-254, and furthermore discussed an apparent systematic discrepancy between stellar model predictions and measurements which is observed for G-K bulge giants. However, in the case of OGLE 2004-BLG-254, it appeared that fitting all data sets together or only a subset of them had an influence on the limb-darkening measurements (Heyrovsky 2008), which remove the observed discrepancy. In order to quantify this effect, we provide in this paper a detailed study on the impact of including data sets on the resulting limb-darkening measurements.

In this work, we model and analyse OGLE 2004-BLG-482, a relatively high-magnification single-lens microlensing event which exhibits clear extended-source effects. The source star fundamental parameters and spectral typing were derived from a high-resolution spectrum obtained on VLT/UVES as part of a ToO programme. A good multi-site and multi-band coverage of the light curve allows us to extract linear limb-darkening coefficients, which we compare to model-atmosphere predictions.

5.2 Photometry – Data Reduction and Analysis

The Galactic microlensing event OGLE 2004-BLG-482 ($l = -0.3392^\circ$, $b = -3.1968^\circ$), or ($\alpha = 17^{\text{h}}57^{\text{m}}30.6^{\text{s}}$, $\delta = -30^\circ51'30''.1$ (epoch J2000.0)) was discovered and publicly alerted on August 8 in 2004 by the OGLE-III¹ Early Warning System (“EWS”, Udalski 2003). The base of it was the observations carried out in the I -filter with the 1.3 m Warsaw Telescope at Las Campanas Observatory (Chile).

Following this alert, the PLANET collaboration (*Probing Lensing ANomalies NETwork*) started its photometric follow-up observations on August 10 (MHJD \simeq 3228), using a network of ground-based telescopes, including the Danish 1.54m (La Silla, Chile), Canopus 1m (Hobart, Tasmania), and Perth/Lowell 0.6m (Bickley, Western Australia) telescopes. Data sets and quasi real-time fitted light curves were made publicly available online², as part of a general data sharing policy. The event was also monitored by the μ FUN collaboration³, which gathered data from six telescopes: the 1.3m and Yale 1.0m (Cerro Tololo Inter-American Observatory, Chile), the Palomar 1.5m telescope (Palomar Observatory, USA), Wise 1m (Mitzpe Ramon, Israel), and two New Zealand amateur telescopes at Auckland (0.35m) and Farm Cove (0.25m).

On August 15 (MHJD \simeq 3233), photometric data indicated a deviation from a normal point-source point-lens light curve. A public alert was issued on August 16, 16:05 UT, pointing toward a high peak magnification event, possibly featuring strong extended-source size effects. In the following hours, on August 17, a Target of Opportunity was activated on the UVES spectrograph at ESO VLT in order to monitor the event peak magnification region where spectroscopic

¹<http://ogle.astrouw.edu.pl>

²<http://planet.iap.fr>

³<http://www.astronomy.ohio-state.edu/~microfun>

effects are expected. Thanks to an almost real-time modelling operated in parallel, the crossing time of the source disk by the lens was estimated to be around 2.4 days. The peak of the light curve was reached on August 18, 18:32 UT at almost three magnitudes above the baseline, corresponding to a minimum (*i.e.* with null blending) peak magnification of $A \sim 15$.

The OGLE data reduction was performed with their own pipeline, implemented for the OGLE III campaigns (Udalski 2003), while PLANET and MicroFUN data were reduced with various versions of the PLANET pipeline (pySIS; Albrow et al. 2009). All these reductions are based on the image subtraction method (Alard & Lupton 1998; Bramich 2008). A preliminary image-quality inspection helped to remove images showing a significant gradient across the field, due to strong background moonlight. Under-exposed images were also removed in this process. We paid particular attention to the quality of data taken at La Silla at the time of peak magnification, because of unfavourable weather conditions at that site. We could however keep a few trusted data points.

After the data reduction process, we set for each PLANET and μ FUN telescope a range of seeing and background within which the homogeneity of the data sets is ensured. For the Yale telescope, we excluded data with seeing outside the range 1.8–3.2". In the case of UTas data, we have applied an upper limit on the seeing of 3.0", and for the Perth, Danish and Auckland telescopes, 3.3". Our final data set and their characteristics are presented in Table 5.1 and the light curve fitted them is displayed in Fig. 5.1.

It is known that error bars we obtain from the data reduction are usually underestimated, and are not homogeneous from one data set to another. To avoid this problem, we rescale the error bars, so that from the best model one has $\chi^2/N \simeq 1$ for each data set fitted alone, with N the corresponding number of data points. We use N instead of d.o.f, because it is not possible to define a proper number of model parameters when fitting multi-site data, as explained in Sec. 5.4.2. This does not affect the results since the data error bars are not Gaussian anyway and d.o.f $\simeq N$ except for Perth. The rescaled error bars σ' then satisfy the following formula

$$\sigma'^2 = (k_\sigma \sigma)^2 + (4 \times -4)^2, \quad (5.1)$$

where k_σ is the rescaling factor. The values of k_σ are listed in Table 5.1, with the corresponding χ^2 per data set for the best-fit model.

5.3 Linear limb-darkening formalism

When the lens resolves the source disk, the light curve shape does contain information not only on the source size ρ_* , but also on its limb-darkening profile, which provides many original stellar application of microlensing.

Limb-darkening profiles of stars can be described analytically at different levels of approximation, in particular by a sum containing powers of $\mu = \cos \alpha$, where α is the angle of a given emerging light ray with respect to the normal of the stellar surface (e.g. Claret 2000). In the most simple case, the so-called the *linear limb-darkening* (hereafter, LLD), which is the first degree of approximation, the star brightness profile can be expressed as

$$I(r) = 1 - a \left(1 - \sqrt{1 - r^2} \right), \quad (5.2)$$

where $r = \sqrt{1 - \mu^2}$ is the fractional radius on the stellar disk from where the light is emitted, and a is the *linear limb-darkening coefficient* (hereafter LLDC). In this work, we will concen-

trate on measuring LLDCs. Firstly, because in microlensing events higher order coefficients have a very small impact (e.g. Dominik (2004) finds that for a caustic crossing, the effect of the change of the LLDC on light curve is ~ 25 times greater than the square-root coefficient). Secondly, because there exists a strong correlation between the coefficients, so it is not possible to precisely measure the LLDC when a further coefficient is taken into account (Kubas et al. 2005). Lastly, because LLDC are widely used and are available in catalogues. It is an important aspect for our goal to compare our results with the literature of stellar limb-darkening.

For our modelling purpose, a more convenient way to rewrite the LLD law is to have a formula which conserves the total source flux for all LLDC values. With this requirement, the LLD law equivalent to Eq. (5.2) but normalised to unit flux can be written as

$$I(r) = \frac{1}{\pi} \left[1 - \Gamma \left(1 - \frac{3}{2} \sqrt{1-r^2} \right) \right], \quad (5.3)$$

where Γ is the LLDC modelling parameter. The value of a can be obtained from Γ thanks to the relation

$$a = \frac{3\Gamma}{2+\Gamma}. \quad (5.4)$$

With this formalism, it is interesting to notice that all limb-darkening profiles intersect at a common fractional radius, $r_{\text{ld}} = \sqrt{5}/3 \simeq 0.75$.

In the following, we make use of Γ for modelling purposes and of a to present our results with comparison to available stellar atmosphere model predictions.

5.4 Modelling

5.4.1 Single-lens, extended-source models

In its motion relative to the lens, the source centre approaches the lens at a minimal distance u_0 in units of the angular Einstein ring radius given by

$$\theta_E = \sqrt{4GMc^{-2}(D_L^{-1} - D_S^{-1})} \quad (5.5)$$

(Einstein 1936) with D_S, D_L the distances from the source and the lens to the observer, M the lens mass, which can be smaller than the source radius ρ_* expressed in the same units. Since high magnification events involve small values of impact parameter u_0 , they are likely to be affected by extended-source effects in particular if the source star is a giant. Although this happens rather rarely in practice (a couple of cases amongst the ~ 700 microlensing events observed every year), this is the case for OGLE 2004-BLG-482.

The point-source magnification at the exact location of the lens is formally infinite, following the well-known formula (Paczynski 1986)

$$A_{\text{pspl}}(u) = \frac{u^2 + 2}{u\sqrt{u^2 + 4}}, \quad (5.6)$$

where u is the distance from the lens to a given point on the source in units of θ_E . Consequently, the flux originating from regions of the source in the immediate neighbourhood of the lens (typically a fraction of the source radius) is preferentially amplified. The relative motion of the source and lens then results in a time-dependent probing of the stellar atmosphere at different fractional radius, corresponding to different optical depths.

Single-lens light curves affected by extended-source effects display a characteristic flattening at their peak. In the case of a uniformly bright extended source, Witt & Mao (1994) derived an exact analytic formula for the magnification which involves elliptic integrals. But there is no similar formula to describe limb-darkened sources, and calculating the exact magnification requires numerical integration. One way is to decompose the source into small rings of uniform intensity. Another approach by Heyrovský (2003) is to perform the angular integration over the stellar disk analytically and only the radial integration numerically, for arbitrary sources.

If some conditions are fulfilled, it is also possible to use approximate formulae, which have the advantage to allow very fast computation. Considering that in Eq. (5.6), $A_{\text{pspl}} \simeq 1/u$ when $u \ll 1$, Yoo et al. (2004) find that the magnification A_{lld} for an extended source with a linear limb-darkening profile with coefficient Γ can be expressed as

$$\begin{aligned} A_{\text{lld}}(u, \rho_*) &= [B_0(z) - \Gamma B_1(z)] A_{\text{pspl}}(u), \\ z &= u/\rho_*, \\ B_0(z) &= \frac{4z}{\pi} E \left[\arcsin \min \left(1, \frac{1}{z} \right), z \right], \\ B_1(z) &= B_0(z) - \frac{3z}{\pi} \int_0^\pi \int_0^1 \frac{r \sqrt{1-r^2}}{\sqrt{r^2 + z^2 - 2zr \cos \phi}} \Gamma \cdot \phi, \end{aligned} \quad (5.7)$$

where E is the incomplete elliptic integral of the second kind. The integral B_1 can be efficiently evaluated and tabulated for z , so can B_0 . This approximation is valid as far as $\rho_*^2/8 \ll 1$ and

$u_0 \ll 1$. Since these relations hold for OGLE 2004-BLG-482 (although close to the limit case of application, since the maximum error for a uniform source here is of the order of 0.2%, but still is much lower than the photometric errors), we choose this formalism.

The complete model then involves four parameters: the source radius ρ_* , as well as u_0 , t_0 and t_E , which define the rectilinear motion of the source with respect to the lens, so that the lens-source separation u satisfies $u^2(t) = u_0^2 + (t - t_0)^2/t_E^2$. Moreover, one has to take into account for each telescope “ i ” two more parameters, the baseline magnitude

$$M_b^i = -2.5 \log(F_S^i + F_B^i) \quad (5.8)$$

and the blending factor $g^i = F_B^i/F_S^i$. Here, F_S^i and F_B^i are respectively the source and the blend flux, the latter referring to any un-magnified flux entering the photometric aperture, from the lens itself and e.g. background stars. They are related to the time-dependent magnification A_{ld} by $F^i(t) = A_{\text{ld}}(t) F_S^i + F_B^i$.

5.4.2 Fitting data

To fit our data sets, we use two minimisation schemes: Powell’s method and a Markov-Chain Monte-Carlo (MCMC) algorithm, from which we also obtain the model parameter error bars (Kains et al. 2009). As stated before, it is not possible to define a proper number of degrees of freedom. In fact, the parameters u_0 , t_0 , t_E and ρ_* are common to all data sets, whereas M_b^i and g^i are associated to the data set “ i ”, and the LLDCs may be chosen to be common per observing filter or per individual telescope. This explains the choice of N instead of d.o.f to rescale the error bars in Sec. 5.2. The first requirement to get precise measurements of limb-darkening coefficients is to get an overall well-covered light curve. This allows us to secure good measurements of the basic parameters u_0 , t_0 , t_E and ρ_* , as well as M_b^i and g^i . The region of the light curve with a noteworthy sensitivity to limb-darkening is, however, mainly limited to when the lens is inside the source-star disk, and drops to a few percent outside. We now discuss this aspect further.

While all limb-darkening profiles intersect at the same fractional radius $r_{\text{ld}} \simeq 0.75$ as seen in Sec. 5.3, the corresponding magnification light curves intersect at around $u_{\text{ld}} \simeq 0.77 \rho_*$ (with u the lens-source centre distance). This special point is marked by a vertical dashed line in Fig. 5.1, in which we also have indicated two other interesting positions of the lens: at the limb of the source ($u = \rho_*$) and at half-way from its centre to its limb ($u = 0.5 \rho_*$). The two dotted magnification curves of the figure show the two extreme cases of LLDC, $\Gamma = 0$ (no limb-darkening) and $\Gamma = 1$. From this we can distinguish three main regions: $0 < u/\rho_* < 0.5$, where the limb-darkening sensitivity is high, up to $\sim 16\%$; $0.5 < u/\rho_* < 0.77$ and $0.77 < u/\rho_* < 1$ where the sensitivity is still of several percent (8% at the limb). Based on this argument and from our data coverage of OGLE 2004-BLG-482 shown in Fig. 5.1, it is then clear that we can expect LLDC measurements from UTas I -band, Danish R -band and Auckland’s clear-filter.

The best-fit parameters and their error bars are given in Table 5.2, Table 5.3 and Table 5.4 for different combinations of data sets. We comment on the results in detail in Sec. 5.7 and 5.8. Fig. 5.1 is plotted for the combined fit including all telescopes and using one coefficient per band.

5.4.3 Estimates of the lens properties

Although the properties of the lens are not of the primary interest in this work, we can still provide an estimate of its mass and distance. However, these quantities cannot be measured here, because an additional observable, such as parallax, is needed to remove a degeneracy between these two parameters. Here, parallax effects are not visible because the time scale of the event is very short, $t_E \simeq 10$ days \ll 1 year.

Instead, we use a Bayesian estimator based on an adequate Galactic model, following Dominik (2006). We find that the lens has a higher probability to be inside the Galactic bulge rather than in the disk (76% vs. 24%), at a distance of $D_L = 7.6_{-0.8}^{+0.5}$ kpc. We estimate its mass to be $M = 0.17_{-0.09}^{+0.17} M_\odot$, which points to a very late red dwarf. This does not contradict the quasi-zero blending we find for the OGLE *I*-band data.

Table 5.1: Final selection of data sets, with the raw number of observational data (frames) and our final selection after the cleaning process. The last column lists the adopted error-bar rescaling factors.

Telescope	Filter	Data	(Frames)	k_σ
UTas (PLANET)	I	86	(128)	2.4
Perth (PLANET)	I	13	(15)	3.8
OGLE	I	44	(68)	2.4
CTIO-Yale (μ FUN)	I	233	(285)	4.2
Danish (PLANET)	R	51	(67)	3.2
Auckland (μ FUN)	(clear)	266	(334)	2.4
All data	—	693	(897)	—

5.5 Calibrated colour-magnitude diagram

The extinction due to the dust/interstellar medium is very significant towards the Galactic bulge. The microlensing event OGLE 2004-BLG-482 took place in OGLE-III field 182.8, which was also observed during the second phase of OGLE (field BUL_SC23) and which photometry is calibrated in I and V filters.

The data were collected when the target was not magnified. From this field ($17' \times 8'$), we extract an I vs. $(V - I)$ colour-magnitude diagram (CMD) by selecting stars surrounding our target within a circle of radius $2.16'$ (500 pixels), which contains around nine thousand objects. This choice ensures that we have enough stars to construct the CMD while keeping a reasonably homogeneous extinction across the selected region. The resulting CMD is presented in Fig. 5.2.

Our target is indicated as the red open triangle and has a calibrated magnitude and colour of $I = 14.41 \pm 0.03$ and $(V - I) = 3.93 \pm 0.04$. Since we find an OGLE blending ratio in I close to zero, and given the fact the object is already very red, it is unlikely to be strongly blended in V as well. We therefore assume in the following no blending, which means the magnitude and colour of the target correspond to those of the source star. We use the ratio of the total to selective extinction $R_I = 1.01 \pm 0.02$ from Sumi (2004) as well as $E(V - I) = 1.41 \pm 0.01$ to get the total extinction $A_I = R_I \times E(V - I) = 1.42 \pm 0.03$, from which we derive the dereddened magnitudes and colour of our target, $I_0 = 13.0 \pm 0.05$, $V_0 = 15.52 \pm 0.04$ and $(V - I)_0 = 2.53 \pm 0.04$.

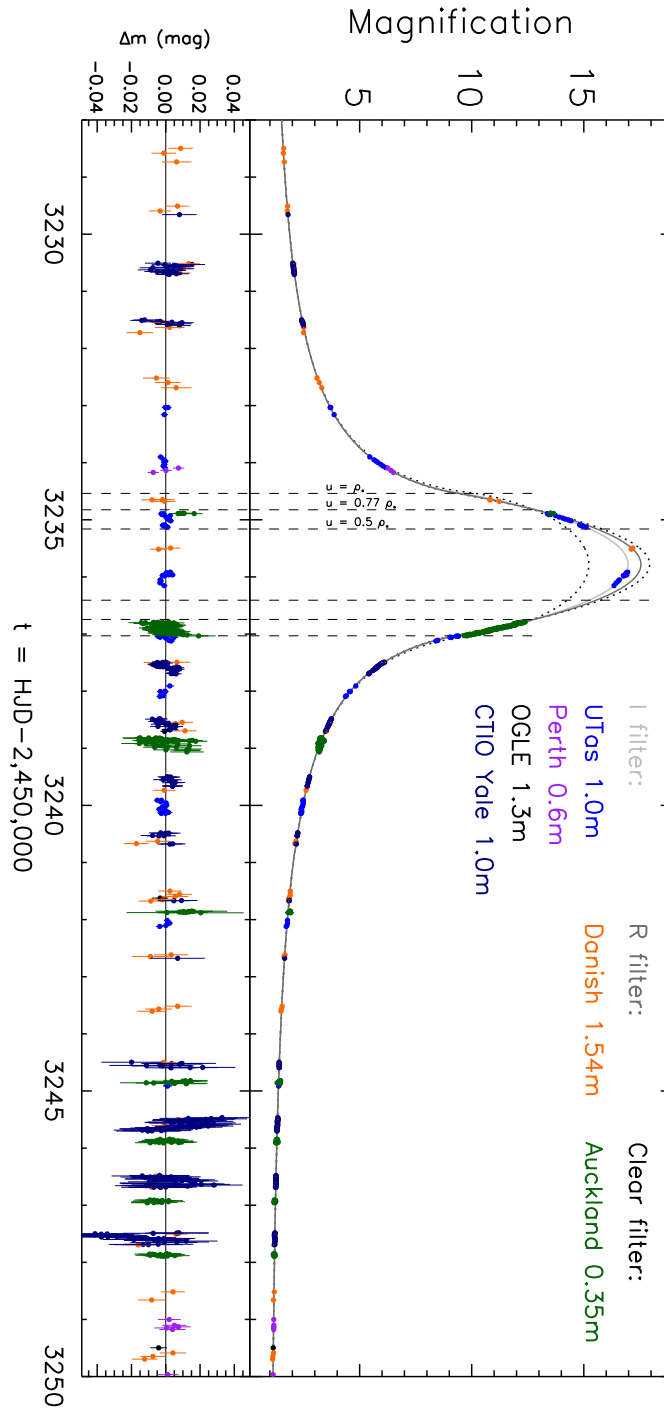


Figure 5.1: Light curve of OGLE 2004-BLG-482, with data from PLANET (Danish, UTas and Perth), OGLE and μ FUN (CTIO-Yale and Auckland) collaborations. The two gray solid lines in the upper panel draw the best-fit model for the *I* and *R* filters with linear limb-darkening parameters given in Table 5.2. The two dotted curves correspond respectively to the two extreme cases, $\Gamma = 0$ (uniformly bright source, lower dotted curve) and $\Gamma = 1$ (upper dotted curve). The two pairs of vertical dashed lines marked $u = \rho_*$ and $u = 0.5 \rho_*$ indicate when the lens is located at the limb of the source and half way from its centre to the limb. All the curves intersect at $u = 0.77 \rho_*$, also marked by a vertical dashed line. The fit residuals in magnitudes are displayed in the lower panel.

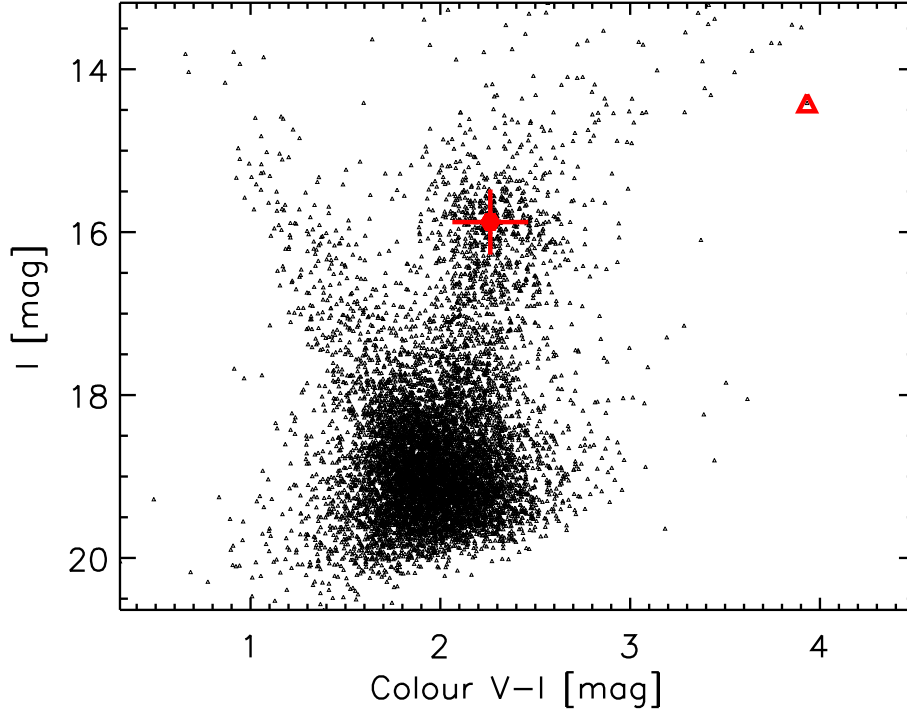


Figure 5.2: OGLE BUL_SC23 field calibrated I vs. $(V - I)$ colour-magnitude diagram, comprising stars within a radius of $2.16'$ centred on our target OGLE 2004-BLG-482 (red open triangle). The red circle indicates the mean position of the RCG centre, and the cross the width of the two-dimensional Gaussian distribution.

The Red Clump Giant (RCG) is marked in Fig. 5.2 as a red circle with error bars. To determine its mean magnitude and colour, we fit a two-dimensional Gaussian around its position (~ 400 stars), from which we derive $I_{\text{RCG}} = 15.88 \pm 0.01$ and $(V - I)_{\text{RCG}} = 2.263 \pm 0.004$. Since its absolute magnitude and intrinsic colour only weakly depend on the star's age and chemical composition, it can be used as distance indicator (Paczynski & Stanek 1998). We adopt for the RCGs mean absolute magnitude the value determined by Stanek & Garnavich (1998) using Hipparcos data, $M_{I,\text{RC}} = -0.23 \pm 0.03$, which recently was confirmed by Groenewegen (2008) with $M_{I,\text{RC}} = -0.22 \pm 0.03$.

For the intrinsic colour, we use the value $(V - I)_{0,\text{RCG}} = 1.01 \pm 0.08$ from Paczynski & Stanek (1998), The mean distance d_{RC} of the RCG is related to these quantities by the relation

$$I_{\text{RCG}} - M_{I,\text{RC}} = 5 \log(d_{\text{RCG}}/\text{kpc}) + 10 + A_{\text{I}}. \quad (5.9)$$

Using this we find a mean RCG distance of $d_{\text{RCG}} = 8.6 \pm 0.2$ kpc. This is not in disagreement with a mean red clump giant located at the Galactic centre, for which the distance is found to be $d_{\text{GC}} = 7.6 \pm 0.3$ kpc according to Eisenhauer et al. (2005) or 7.9 ± 0.7 kpc according to Groenewegen et al. (2008). We actually expect d_{RCG} to be slightly larger than d_{GC} in this field, due to the Galactic bar geometry and the negative longitude of OGLE 2004-BLG-482. Nevertheless, it is likely that the difference we find is mainly due to an uncertainty in the absorption

A_I we are using, since there are still many unknowns related to this topic. In the following, we adopt a source star distance of $d = 8 \pm 1$ kpc, assuming the same reddening as for the RCG.

We fit calibrated isochrones from Bonatto et al. (2004) to Two Micron All-Sky Survey (2MASS) data, from which we derive the near-infrared extinctions $A_J = 0.52 \pm 0.10$, $A_H = 0.36 \pm 0.11$ and $A_{K_s} = 0.20 \pm 0.02$. From this and the absorption corresponding to our target in the 2MASS database (2MASS 17573061-3051305), we get $J_0 = 11.55 \pm 0.10$, $H_0 = 10.68 \pm 0.11$ and $K_{s,0} = 10.42 \pm 0.04$, as well as the corresponding colours $(J - H)_0 = 0.87 \pm 0.16$, $(H - K_s)_0 = 0.26 \pm 0.12$ and $(J - K_s)_0 = 1.13 \pm 0.11$. This allows us to estimate the source radius using the surface brightness relation

$$\log \theta_* + V_0/5 = (0.24 \pm 0.01) \times (V - K)_0 + (0.61 \pm 0.03) \quad (5.10)$$

from Groenewegen (2004) and which is valid only for M giants, where θ_* is the source angular diameter in *mas* and $(V - K)_0 = V_0 - (K - A_K) = 5.10 \pm 0.06$ (assuming $K \simeq K_s$). We find an angular diameter of $\theta_* = 51.8 \pm 8.2 \mu\text{as}$, and with the adopted source distance of $d = 8 \pm 1$ kpc we find a physical source radius of $R_* = 45 \pm 9 R_\odot$.

From a pure photometric point of view, $(V - I)_0$ and near-infrared colours point toward an M4 III according to Bessell & Brett (1988), and to an M5.5 III according to Houdashelt et al. (2000). Such discrepancies between authors on spectral typing based on photometric measurements is already known. In the next section, we perform the analysis of the VLT/UVES high resolution spectra we obtained on this event, in order to derive more accurately the spectral type and to determine the fundamental parameters of the source star.

5.6 Source star properties from the photometry and spectroscopy

In the Galaxy the light emitted by source stars is affected by interstellar medium along the line of sight due to absorption. The spectrum for the stellar source of OGLE 2004-BLG-482 we obtained with the high-resolution optical spectrograph UVES (Ultraviolet and Visible Echelle Spectrograph) installed at the ESO Very Large Telescope (VLT), on mount Paranal (Chile). It was performed as a part of a Target of Opportunity activated shortly after the peak of the light curve was passed. The data were reduced in a standard way using version 2.1 of the UVES context of the MIDAS data reduction software.

Absorption lines from source stars can be analysed to determine their physical properties such as the effective temperature, the surface gravity and metallicity/ chemical abundance. The absorption lines apparent in the presented spectrum, Fig. 5.3 It makes possible to determine the spectral type of source star. The spectrum of OGLE 2004-BLG-482 is dominated by broad absorption bands from molecules. The shape and depth of molecular absorption bands, particularly TiO, are very sensitive to the stellar effective temperature T_{eff} , and in a small degree also to the surface gravity $\log g$, we estimated the atmospheric parameters of OGLE 2004-BLG-482 by comparing the observed spectrum with a grid of pre-calculated synthetic template spectra.

The grid of synthetic template spectra, calculated by Plez (priv. comm.), is based on synthetic spectra calculated from MARCS model atmospheres (Gustafsson et al. 2008, 2003, 1975; Plez et al. 2003, 1992), and includes the latest available atomic and molecular line data (Gustafsson et al. 2008; Kupka et al. 1999; Plez 1998). Synthetic template spectra for M giants calculated with the MARCS model atmospheres have a good record for determining stellar

5.6. SOURCE STAR PROPERTIES FROM THE PHOTOMETRY AND SPECTROSCOPY 53

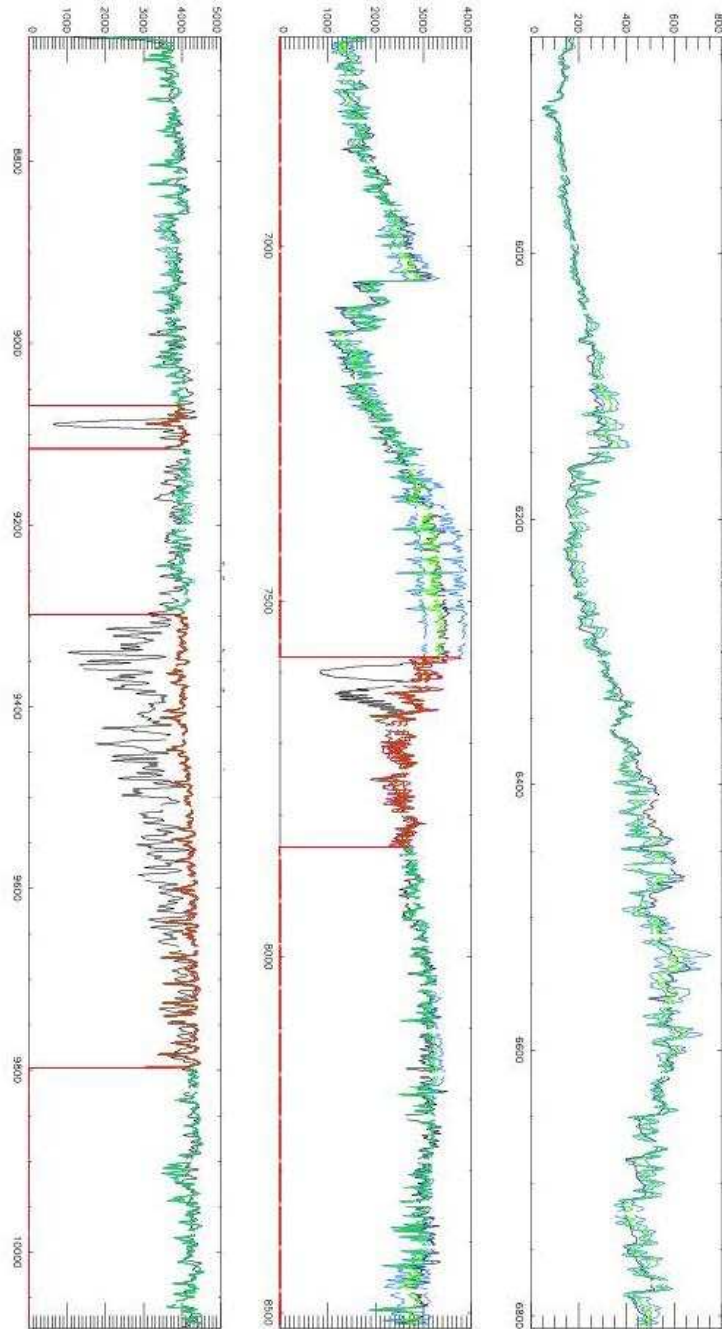


Figure 5.3: The observed (black line) and best-fit (green) template spectrum of the OGLE 2004-BLG-482 microlensing event. The region around the TiO 7100 shows the agreement of the observed and synthetic spectra. Besides two curves (blue) are plotted at ± 100 K. The regions excluded from the fit are indicated in red.

parameters in M super giants (e.g. Levesque et al. 2005, 2007; Massey et al. 2008) and were extensively used to calibrate M giant photometry (Bessell et al. 1998).

The grid used in our analysis covers an effective temperature range of $3000\text{K} < T_{\text{eff}} < 4000\text{K}$, with steps of 100 K, and a surface gravity range of $0.0 < \log g < 3.0$, with steps of 0.5. This grid was calculated for giants with solar abundances and no carbon enrichment. Since our grid does not cover a range of metallicities, we therefore have no leverage on this parameter. We also prepared routines to calculate linear interpolations between the spectra in our grid for any given value of T_{eff} and $\log g$.

We then compared the observed spectrum of OGLE 2004-BLG-482 with template spectra across the available range of T_{eff} and $\log g$ and determined the goodness-of-fit using the χ^2 diagnostic. In calculating χ^2 , we used the entire observed spectrum, from approximately 4800 to 10000 Å, only excluding three regions that are strongly affected by telluric absorption (7580–7850, 9070–9120 and 9300–9800 Å). However, since no continuum is present in our spectrum, and we also do not know the absolute stellar flux, we renormalised the synthetic spectrum using a one-dimensional polynomial function prior to calculate χ^2 . This renormalization does not affect the shape of the broad molecular bands that are important for determining T_{eff} and $\log g$.

We refined the best values of T_{eff} and $\log g$ using parabolic minimisation between the grid points that yielded the lowest value of the χ^2 diagnostic. In Fig. 5.3 we illustrate the agreement between the observed and best-fit template spectrum, including estimated parameter uncertainties, around the highly temperature-sensitive TiO band near 7100 Å. We find that the parameters that best fit our observed spectrum are $T_{\text{eff}} = 3667 \pm 150\text{K}$ and $\log g = 2.1 \pm 1.0$, assuming solar abundances. The quoted error bars are dominated by systematic uncertainties in the synthetic spectra and data reduction procedures used, such as flux calibration. Our uncertainties are further increased due to the fact that our grid of template spectra was calculated for only one metallicity. The range of effective temperatures we find is compatible with a star of MK spectral type between M1 and M5, with the best-fit value giving a red giant star a bit later than M3 (Houdashelt et al. 2000; Strassmeier & Schordan 2000).

The large error bar on the surface gravity confirms that our spectrum has little to offer in gravity-sensitive diagnostics. We can however obtain independent constraints on $\log g$: given that the mass of an M giant of 1 or 10 Gyr is smaller than 2.3 and $1M_{\odot}$ respectively, using $\log g = \log g_{\odot} + \log M - 2 \times \log R_*$, we find the corresponding upper limits of the surface gravity: $\log g = 1.5 \pm 0.2$ and $\log g = 1.1 \pm 0.2$ respectively, taking into account the uncertainty on the source radius. This is in agreement with our spectroscopic analysis, although favouring the lower boundary.

5.6.1 Conclusion on the source MK type and parameters

We finally find a good agreement between our photometric and spectroscopic study, with a source star of MK spectral type a bit later than M3. We therefore adopt the fundamental parameters from the spectroscopic analysis ($T_{\text{eff}} = 3667 \pm 150\text{K}$, $\log g = 2.1 \pm 1.0$, solar metallicity) to make our selection of atmosphere models used to compare our limb-darkening measurements to model predictions, as discussed in the next section.

Table 5.2: Model parameters and error bars for independent fits for U, D and A data sets. The measured linear limb-darkening coefficients are indicated in bold face. The data sets are referred to by letters, following the convention indicated in the first line of the table. Models for which no stable fit or very unrealistic results are obtained are marked with the symbol “[*]” following the measured value.

Parameters	UTAS (U)	DANISH (D)	AUCKLAND (A)	OGLE (O)	PERTH (P)	CTIO (C)	YALE
<i>Independent fits for U, D and A</i>							
t_0 (days)	3235.78(4 ± 1)	3235.78(3 ± 3)	3235.76(8 ± 4)	–	–	–	–
u_0	0.010(8 ± 4)	0.0(2 ± 1)	0.0(0 ± 1)	–	–	–	–
t_E (days)	8.(9 ± 1)	9.(6 ± 4)	9.(3 ± 3)	–	–	–	–
ρ_*	0.14(0 ± 2)	0.1(3 ± 1)	0.14(0 ± 7)	–	–	–	–
a	0.677 ± 0.013	0.67 ± 0.22 [*]	0.76 ± 0.13	–	–	–	–
M_b	11.5	11.4	13.5	–	–	–	–
g	7.0	1.4	4.5	–	–	–	–
χ^2	82.5	43.2	234.9	–	–	–	–

Table 5.3: Model parameters and error bars for different relevant combinations of data sets. The measured linear limb-darkening coefficients are indicated in bold face. The data sets are referred to by letters, following the convention indicated in the first line of the table. Models for which no stable fit or very unrealistic results are obtained are marked with the symbol “[*]” following the measured value.

Parameters	UTAS (U)	DANISH (D)	AUCKLAND (A)	OGLE (O)	PERTH (P)	CTIO (C)	YALE
<i>Combined fit including U+D</i>							
t_0 (days)	3235.784(5 ± 8)						
u_0	0.00(9 ± 2)						
t_E (days)	9.1(5 ± 9)						
ρ_*	0.13(7 ± 1)						
a	0.674 ± 0.012	0.837 ± 0.018	–	–	–	–	–
M_b	11.5	11.4	–	–	–	–	–
g	7.2	1.3	–	–	–	–	–
χ^2	85.1	57.8	–	–	–	–	–
<i>Combined fit including U+A</i>							
t_0 (days)	3235.780(8 ± 8)						
u_0	0.00(0 ± 3)						
t_E (days)	9.(1 ± 1)						
ρ_*	0.13(8 ± 2)						
a	0.714 ± 0.013	–	0.660 ± 0.023	–	–	–	–
M_b	11.5	–	13.5	–	–	–	–
g	7.2	–	4.5	–	–	–	–
χ^2	101.9	–	286.3	–	–	–	–
<i>Combined fit including D+A</i>							
t_0 (days)	3235.77(5 ± 3)						
u_0	0.00(0 ± 7)						
t_E (days)	9.(7 ± 2)						
ρ_*	0.13(4 ± 8)						
a	–	1.0 ± 0.23 [*]	0.93 ± 0.29 [*]	–	–	–	–
M_b	–	11.4	13.5	–	–	–	–
g	–	1.4	4.8	–	–	–	–
χ^2	–	50.6	241.5	–	–	–	–

Table 5.4: Model parameters and error bars for different relevant combinations of data sets. The measured linear limb-darkening coefficients are indicated in bold face. The data sets are referred to by letters, following the convention indicated in the first line of the table. Models for which no stable fit or very unrealistic results are obtained are marked with the symbol “[*]” following the measured value.

Parameters	UTAS (U)	DANISH (D)	AUCKLAND (A)	OGLE (O)	PERTH (P)	CTIO (C)	YALE
<i>Combined fit including U+D+A</i>							
t_0 (days)	3235.781(4 ± 9)						
u_0	0.00(0 ± 4)						
t_E (days)	9.2(9 ± 6)						
ρ_*	0.13(6 ± 1)						
a	0.713 ± 0.012	0.881 ± 0.010	0.660 ± 0.011	–	–	–	–
M_b	11.5	11.4	13.5	–	–	–	–
g	7.3	1.3	4.6	–	–	–	–
χ^2	102.7	58.1	287.8	–	–	–	–
<i>Combined fit including all telescopes (one LLDC per band)</i>							
t_0 (days)	3235.781(6 ± 7)						
u_0	0.00(0 ± 2)						
t_E (days)	9.6(1 ± 2)						
ρ_*	0.130(9 ± 5)						
a	0.714 ± 0.010	0.884 ± 0.021	0.652 ± 0.016	0.714 ± 0.010	0.714 ± 0.010	0.714 ± 0.010	0.714 ± 0.010
M_b	11.5	11.4	13.5	14.1	12.7	14.0	–
g	7.6	1.4	4.8	0.0	0.7	–0.8	–
χ^2	122.7	51.0	286.6	42.6	14.3	239.7	–

5.7 Discussion of the linear limb-darkening coefficients

As discussed in Sec. 5.4.2, three data sets have some sensitivity to limb-darkening: UTas (*I*-band), Danish (*R*-band) and Auckland (clear filter). The first question we address now is how the individual limb-darkening coefficients (LLDC) are affected by including or removing some of our data sets. In fact, our first step was to model every data set independently, and step by step to include other telescopes. We first note that there is a change in the LLDC values which depends on the added data sets. We thus performed a detailed analysis to understand what could cause such variations, and to identify combinations of data sets which lead to proper LLD measurements. The results we are commenting are presented in Fig. 5.4: the three columns correspond to UTas, Danish and Auckland respectively, and the individual panels display the LLDC measurements for various combinations of data sets. The corresponding model parameters are given in Table 5.2 for independent fits for UTas, Danish and Auckland data sets, and in Table 5.3 and Table 5.4 for combined fits. In the figure and tables, the letters A, C, D, O, P, U refer respectively to the telescopes Auckland, CTIO Yale, Danish, OGLE, Perth and UTas.

UTas (U) clearly provides the best data set for LLDC measurements, since the data sample the whole LLD-sensitive region at the peak of the light curve, as well as its wings and baseline. On the other hand, modelling Danish (D) alone provides a very unrealistic fit, with large error bars and very irregular MCMC correlations. This result cannot be trusted. To explain this, we recall that as mentioned in Sec. 5.2, the peak of the light curve was observed under bad weather conditions in La Silla, in particular the two consecutive data points around $t = 3235.5$. Moreover, the data coverage is not optimal since there are only two epochs which cover the LLD-sensitive part of the light curve. As a result, this lack of good coverage combined with some uncertainty in the data lead to many local minima (which can be seen by running a MCMC), and amongst these the fitting converges towards an unrealistic solution. As we shall see later, adding other data sets can nevertheless help stabilise the fit. The last telescope with data sensitive to limb-darkening is Auckland (A). We can fit the corresponding data alone and obtain a reasonable fit, but we obtain large error bars because the photometric accuracy of the data is a few times lower than for UTas, and furthermore, the data taken during the source crossing are all located close to the limb, in the region of less sensitivity to limb darkening. We note that the LLDC we obtain is higher than UTas's, which is expected, since Auckland's clear filter is known to peak between red and infrared and LLDCs usually decrease towards infrared.

Starting from these models, we include different combinations of other data sets. If we base our analysis on the LLDC measurement from our best data set, UTas, then we find two distinct behaviours: either the UTas's LLDC is not displaced from the individual fit ($a \simeq 0.67$, here U+D) or is slightly modified ($a \simeq 0.71$, e.g. U+A or all telescopes). Interestingly, in the single case where UTas's LLDC is not changed, which corresponds to a combined fit with data from the Danish, we obtain a reasonable measurement of the Danish's LLDC as well. We interpret this as a stabilisation of the Danish fit by UTas data, which helps eliminate ambiguous local minima previously spotted. Combining Auckland with UTas or any other data set moves the value of UTas's LLDC. We also note that no reasonable fit can be obtained by fitting Auckland and Danish together (no stabilisation).

From this, we conclude that a precise measuring of LLDC requires a very careful study: first, one has to identify the data sets which can potentially provide a limb-darkening measurement with enough sensitivity, based on the light-curve sampling as discussed in Sec. 5.4.2. Then, one has to check whether the inclusion of additional data sets affects the results. In fact,

as we have shown for this microlensing event, adding more data sets to the light curve modelling can lead to two opposite effects: either the new data stabilise the fit and help obtain LLDCs for more data sets, or on the contrary perturb the LLDC measurements. The latter may happen if unknown systematic effects are affecting the data, or if the data have a stronger sensitivity to other non-modelled physical effects. Moreover, from the different fits we performed using different rescaling factors or data reductions, we find that the best-fit parameters change a bit more than what can be expected from the found error bars, which means the latter are somehow underestimated.

In the case of OGLE 2004-BLG-482, the most reliable LLDCs come from combining UTas and Danish (U+D), while using Auckland alone is the best choice to measure its LLDC (in fact, if combined with UTas or Danish, Auckland modifies their LLDC values). The relevant measurements we discuss below are marked in Fig. 5.4 with a black square in the upper right of the corresponding panels. When the fit is performed using the formula of Heyrovský (2003), we obtain similar results for the combinations U+D and A: $a_U = 0.655^{+0.010}_{-0.016}$, $a_D = 0.825^{+0.023}_{-0.022}$ and $a_A = 0.751^{+0.083}_{-0.010}$.

In order to compare our measurements to linear limb-darkening predictions from atmosphere models, we use two sets of LLDC computed from Kurucz's ATLAS models (e.g. Kurucz 1992, 1994). The first set of LLDC are taken from Claret (2000), using the VizieR database, for the whole available range of temperatures and $\log g$ compatible with OGLE 2004-BLG-482's source star fundamental parameters (Sec. 5.6); we assume a solar metallicity to be consistent with our spectral analysis. The corresponding LLDCs are plotted in Fig. 5.4 as thin, open hexagons. The number of models corresponding to our requirements amounts to twelve: two different temperatures (3500 and 3750 K), three $\log g$ (1.0, 1.5 and 2.0, plotted from smaller to bigger symbols) and for each configuration two microturbulent velocities (1 and 2 km/s). The second set of LLDCs is plotted as filled diamonds, and correspond to coefficients computed using the interpolation method advocated by Heyrovský (2007). These are computed for the same stellar parameters as previously.

As one can see, our LLDC measurements are in very good agreement with the predictions from atmosphere models. For UTas I , our measurement is compatible with both the predictions from Claret (2000) and Heyrovský (2007). For the Danish R filter, the agreement is also very good, although our measurement is slightly larger than the prediction. For the Auckland clear filter, only Heyrovský (2007) predictions are available; but within the large error bars commented on previously, the data are compatible with the predictions.

5.8 Principal Components Analysis

Although analytical laws are usually used to model the star's limb-darkening, other possible options are to use non-parametric models, or to build a new basis functions directly from model-atmosphere limb-darkening profiles. We use a limb-darkening basis numerically constructed by principal component analysis (PCA, and PCA LD in the following) for a set of given model atmosphere limb-darkening profiles, following Heyrovský (2003).

In this approach, the stellar intensity profile is expressed as

$$I(r) = \sum_i \alpha_i f_i(r), \quad (5.11)$$

in place of Eq. (5.2), where the f_i are the PCA basis functions and α_i are weighting coefficients. In the case of OGLE 2004-BLG-482, 120 ATLAS models Kurucz (1992) were used to perform the PCA, with $T_{\text{eff}} = 3500, 3750$ and 4000 K, $\log g = 1.0, 1.5, 2.0, 2.5$ and 3.0 dex, $[Fe/H] = -0.3, -0.2, -0.1,$ and 0.0 dex and a microturbulent velocity of $v_t = 2.0$ km/s (Heyrovsky 2008). The resulting first three components $f_{i \in [1,2,3]}$ are displayed in Fig. 5.5.

In the simplest case of a 2-term PCA LD (the analogue to the analytical linear limb-darkening law, LLD), the relevant parameter which drives the star’s brightness profile is $\kappa \equiv \alpha_2/\alpha_1$. All possible shapes are obtained by varying κ in the range $-0.161 \lesssim \kappa \lesssim 0.09$, from the most peaked to the flattest limb-darkening profiles.

We perform the fitting using Heyrovský (2003) formalism, for different combinations of data sets in a similar way as in Sec. 5.7. The results are presented in Fig. 5.6, for the combinations of data sets which were selected in the previous section (panels with a black mark in the upper right of Fig. 5.4).

As for the classical LLD law commented in details in the previous section, we find a very good agreement between model predictions and our measurements. This shows that PCA LD provides an interesting alternative to model stellar brightness profiles. Since by construction PCA LD better fit atmosphere model limb darkening (Heyrovsky 2008), they can be of particular interest to model light curves where stellar limb darkening is a “nuisance” effect rather than a primary study target (e.g. planetary microlensing, Kubas et al. 2008) in order to limit systematic errors coming from it. On the other hand, one of its drawbacks is that it requires to perform a principal component analysis on a set of selected atmosphere models, which should match as well as possible the stellar parameters of the star. Finally, because they match very well the atmosphere model limb-darkening profiles, PCA LD strongly depends on our current understanding of stellar atmospheres. This means that if the atmosphere models used lack a proper description of physical processes (*cf.* Sec. 5.1), the derived PCA LD laws will be inappropriate, but conversely it provides a unique flexibility in including further features in the models that will be reflected in the limb-darkening profiles, compared to the rigidity of the classical analytical LD laws.

5.9 Summary and Conclusion

In this chapter we performed a detailed study of OGLE 2004-BLG-482, a relatively high-magnification single-lens microlensing event with clear extended-source effects, which was densely covered by our telescope networks. It provided us with the rather rare opportunity to directly test model-atmosphere limb-darkening predictions for the source star. Such a comparison was made possible because we could obtain high-resolution UVES spectra at VLT at a critical time thanks to the short activation of a ToO programme at VLT, from which we could precisely estimate the star’s fundamental parameters. The source typing has been confirmed at a good precision level by our photometric diagnostic based on a calibrated colour-magnitude diagram of the field. We have performed a very detailed modelling to evaluate the impact of including data sets in the modelling process, and provide new diagnostics for future work.

We find the measured limb darkening agrees very well with model-atmosphere predictions, both when considering linear limb-darkening laws, or alternative limb-darkening profiles based on a principal component analysis of ATLAS stellar atmosphere models. From this study in which the precision has been pushed at high level, we conclude that this late M giant does

not suffer from any clear discrepancy between limb-darkening model predictions and measurements, which has been pointed out for earlier K giants. Although it is based on the observation of a single event, it is very likely that the conclusion can be extended to similar late M giants.

The contents of this chapter will be published in the article (Zub, M., Cassan, A., Heyrovský, D., et al. 2009) submitted to *Astronomy & Astrophysics*.

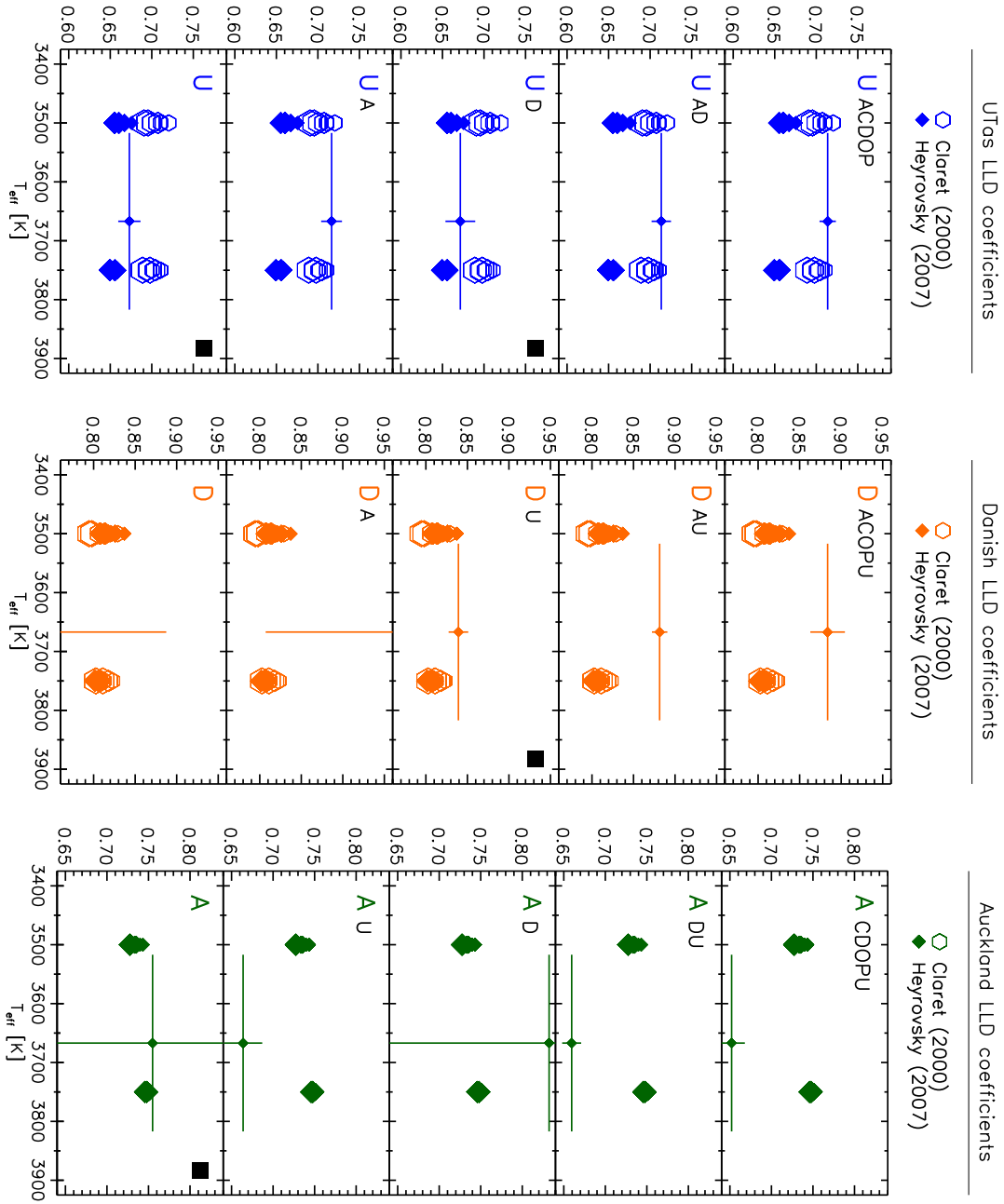


Figure 5.4: Graphical representation of the linear limb-darkening measurements (crosses) for the three data sets with sensitivity to limb-darkening: UTas in the I -band, Danish in the R -band and Auckland in a clear filter. The open hexagons and the filled diamonds are respectively the predictions from Claret (2000) and Heyrovský (2007) linear limb-darkening (LLD) coefficients. The fitting of the light curve is performed for different combinations of telescopes (same letter conventions as for Table 5.2), and the results are discussed in Sec. 5.7. The adopted measurements are those marked with black squares in the upper right of the panels.

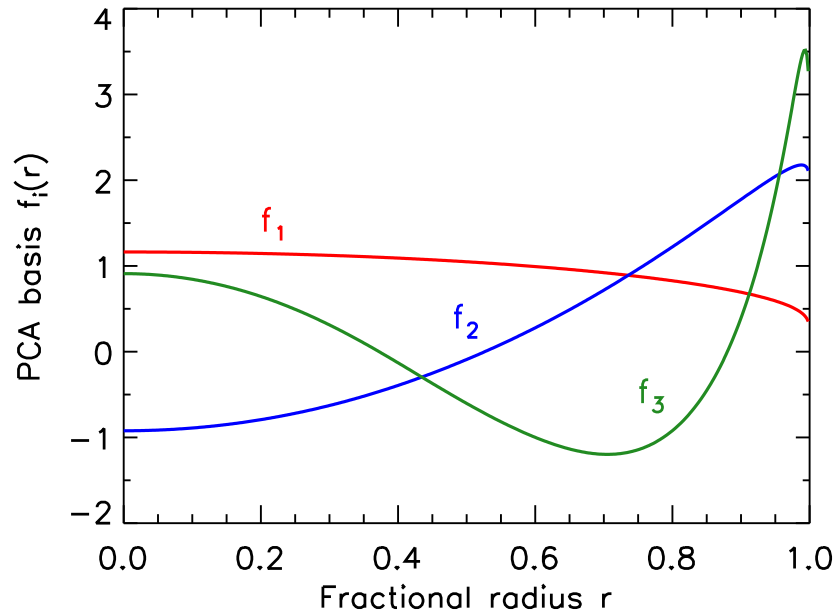


Figure 5.5: The first three components of the PCA basis, computed for a set of given model atmosphere limb-darkening profiles which match the fundamental stellar parameters of OGLE 2004-BLG-482’s source star.

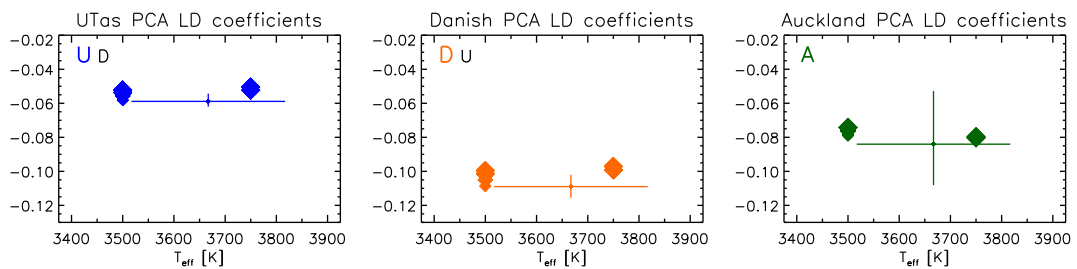


Figure 5.6: Limb-darkening (LD) coefficients κ measured (crosses) and predicted (diamonds, Heyrovsky 2008) using the 2-term PCA LD as explained in the text. Letters and colours have the same meaning as in Fig. 5.4. The chosen vertical axis range is a zoom of the full possible variation for κ , which is $-0.161 \lesssim \kappa \lesssim 0.09$.

Chapter 6

Conclusions and Prospects

I did my PhD as a member of the international collaboration PLANET which aim is to monitor anomalous microlensing events towards the Galactic bulge. I took part in the observation campaigns (four observing runs, in Chile and South Africa), and dedicated a substantial amount of time to data reduction, analysis and modelling of promising targets. In particular, I led two main projects as a core part of my work: modelling of six high magnification microlensing events to search for extrasolar planets, and analysing the microlensing event OGLE 2004-BLG-482 to study the atmosphere of its Galactic bulge giant source star.

In the first main project, we reviewed all high magnification events observed during the 2006 season in order to select a well-covered subset of events which could hide a planetary signal. We found six interesting candidates, including two for which we suspected a possible planetary signal (OGLE 2006-BLG-245 and MOA 2006-BLG-099). We therefore performed a very careful data reduction, modelling and analysis to search for low mass planetary companions of the lens star. Although the detection efficiency is high for such high magnification events, no signal passed our detection criteria. Hence we were able to exclude such kind of planetary candidates from the 2006 observations. In the second main project, we have performed a very detailed data reduction, modelling and analysis of OGLE 2004-BLG-482, a single-lens microlensing events showing clear extended-source effects. Although relatively rare, these events provide a unique opportunity to obtain very precise information on the source star's brightness profile. We first performed a careful reduction of data coming from eleven telescopes from the PLANET, OGLE and MicroFUN collaborations, and selected those with enough photometric precision for our goal. A detailed modelling focused on the measurement of linear limb-darkening coefficients led to precise value for coefficients in three bands. We provided new diagnostics that allow us to tell which kind of data coverage may lead to precise limb-darkening measurements. Thanks to VLT/UVES spectra taken as part of a ToO programme, we could also measure the star's fundamental parameters, $T_{\text{eff}} = 3667 \pm 150\text{K}$ and $\log g = 2.1 \pm 1.0$, which agreed to the OGLE colour-magnitude diagram we had for this star, a M3 cool giant. From these source characteristics, we obtained in the literature corresponding model-atmosphere predicted limb-darkening coefficients, that we compared to our measurements. We found a very good agreement, from which we concluded that stars of this type do not suffer from a discrepancy between models and observations which was found in the case of G/K giants.

In the last few years, gravitational microlensing has proven to be an efficient method to detect low-mass planets, especially “Super-Earth” planets at many astronomical units from their parents stars. Although the 2006 season did not provide any planet by the detection channel of high magnification microlensing events, a couple of such discoveries in other observing seasons suggest that the detection rate will highly increase in the coming years. Besides the better communication between the survey teams OGLE and MOA, the competitive follow-up collaborations PLANET and MicroFUN will merge for the 2009 season, with a complementary observational strategy, more telescopes and an improved organisation. There is no doubt this will be a new step in the efficiency of finding planets, at orbital separations where no other method can probe the low-mass planets populations. In the near future, the one-meter class telescopes are to be replaced by two-meter class telescopes with wide fields of view. It will then become possible to operate at the same time on a given telescope the survey of millions of targets and the follow-up of interesting ones, with a 24 hours continuous observing thanks to the network setup.

The intrinsic sensitivity of the microlensing technique is not limited to planets of few times that of the Earth. In fact, bodies with masses down to a fraction of it are at reach in favourable conditions. Microlensing is thus more than ever still in the race of which method will find the first extrasolar ‘Earth’.

Publications List

Zub, M., Cassan, A., Heyrovský, D., Fouqué, P., Stempels, H.C., and 46 coauthors:
"Limb-darkening measurements for a cool red giant in microlensing event OGLE 2004-BLG-482",
submitted to Astronomy & Astrophysics, 2009

Kains, N., Cassan, A., Horne, K., Albrow, M. D.,..., **Zub, M.**, and 40 coauthors:
"A systematic fitting scheme for caustic-crossing microlensing events",
2009, MNRAS, (in press), astro-ph/arXiv:0901.1285

Southworth, J., Hinse, T.C., Joergensen, U.G., Dominik, M.,..., **Zub, M.**, and 18 coauthors:
"High-precision photometry by telescope defocussing. I. The transiting planetary system WASP-5",
2009, MNRAS, (in press), astro-ph/arXiv:0903.2139v1

Albrow, M. D., Horne, K., Bramich, D. M., Fouqué, P.,..., **Zub, M.**, and 22 coauthors:
"Difference imaging photometry of blended gravitational microlensing events with a numerical kernel",
submitted to MNRAS, 2009

Kubas, D., Cassan, A., Dominik, M., Bennett, D.P.,..., **Zub, M.**, and 30 coauthors:
"Limits on further planetary companions to OGLE 2005-BLG-390L",
2008, Astronomy & Astrophysics, **483**, 317

Fynbo, J.P.U., Watson, D., Thöne, Ch.C., Sollerman, J.,..., **Zub, M.**, and 26 coauthors:
"No supernovae associated with two long-duration γ -ray bursts",
2006, Nature, **444**, 1047

List of Figures

2.1	Light deflection due to the gravitational potential.	6
2.2	Geometric description of gravitational microlensing.	7
2.3	Source images for a single-lens case	8
2.4	Point-source, point-lens light curves	11
2.5	The topologies of binary lenses	12
3.1	The Galactic bulge	16
3.2	The location of the PLANET telescopes	17
3.3	Findig chart of OGLE 2004-BLG-482	20
4.1	Light curve of OGLE 2006-BLG-265 microlensing event	27
4.2	Light curve of OGLE 2006-BLG-416 microlensing event	28
4.3	Light curve of OGLE 2006-BLG-229 microlensing event	29
4.4	Light curve of OGLE 2006-BLG-440 microlensing event	30
4.5	Light curve of OGLE 2006-BLG-245 microlensing event	33
4.6	Central part of OGLE 2006-BLG-245 light curve.	34
4.7	Light curve of MOA 2006-BLG-099 event	37
4.8	Central part of MOA 2006-BLG-099 light curve.	38
5.1	Magnification curve of OGLE 2004-BLG-482	50
5.2	Apparent magnitude versus colour diagram relevant to OGLE 2004-BLG-482	51
5.3	The observed and best-fit template spectrum of OGLE 2004-BLG-482	53
5.4	Linear limb-darkening coefficients (LLDC) in the I -, R -band and in a clear filter	62
5.5	The first three components of the PCA basis	63
5.6	PCA limb-darkening coefficients in the I -band	63

List of Tables

3.1	Data reduction parameters for OGLE 2004-BLG-482	19
4.1	The summary of the high magnification events selection	25
4.2	Data set of OGLE 2006-BLG-245	32
4.3	Best fit model parameters of OGLE 2006-BLG-245	32
4.4	Data set of MOA 2006-BLG-099	35
4.5	Best fit model parameters of MOA 2006-BLG-099	36
5.1	Final selection of the OGLE 2004-BLG-482 data sets	48
5.2	Model parameters and error bars for independent fits for U, D and A data sets .	55
5.3	Model parameters and error bars for combined fits including U+D, U+A, D+A	56
5.4	Model parameters and error bars for combined fits including U+D+A and all sets	57

Bibliography

- Abe, F., Bennett, D. P., Bond, I. A., et al. 2003, *A&A*, 411, L493 5.1
- Afonso, C., Alard, C., Albert, J. N., et al. 2000, *ApJ*, 532, 340 5.1
- Afonso, C., Albert, J. N., Andersen, J., et al. 2001, *A&A*, 378, 1014 5.1
- Alard, C. & Lupton, R. H. 1998, *ApJ*, 503, 325 3.2, 3.3, 5.2
- Albrow, M., Horne, K., Bramich, D., et al. 2009, submitted to *MNRAS* 5.2
- Albrow, M. D., An, J., Beaulieu, J.-P., et al. 2001, *ApJ*, 549, 759 5.1
- Albrow, M. D., Beaulieu, J.-P., Caldwell, J. A. R., et al. 1999a, *ApJ*, 512, 672 5.1
- Albrow, M. D., Beaulieu, J.-P., Caldwell, J. A. R., et al. 2000, *ApJ*, 534, 894 5.1
- Albrow, M. D., Beaulieu, J.-P., Caldwell, J. A. R., et al. 1999b, *ApJ*, 522, 1011 5.1
- Alcock, C., Akerloff, C. W., Allsman, R. A., et al. 1993, *Nature*, 365, 621 1
- Alcock, C., Allen, W. H., Allsman, R. A., et al. 1997, *ApJ*, 491, 436 5.1
- An, J. H., Albrow, M. D., Beaulieu, J.-P., et al. 2002, *ApJ*, 572, 521
- Aubourg, E., Bareyre, P., Brehin, S., et al. 1993, *Nature*, 365, 623 1
- Beaulieu, J.-P., Bennett, D. P., Fouqué, P., et al. 2006, *Nature*, 439, 437 4.1
- Bennett, D. P., Bond, I., Cheng, E., et al. 2004, in *Bulletin of the American Astronomical Society*, Vol. 36, *Bulletin of the American Astronomical Society*, 1356–+
- Bennett, D. P., Bond, I. A., Udalski, A., et al. 2008, *ApJ*, 684, 663 1
- Bennett, D. P. & Rhie, S. H. 1996, *ApJ*, 472, 660 4.1
- Bessell, M. S. & Brett, J. M. 1988, *PASP*, 100, 1134 5.5
- Bessell, M. S., Castelli, F., & Plez, B. 1998, *A&A*, 333, 231 5.6
- Bonatto, C., Bica, E., & Girardi, L. 2004, *A&A*, 415, 571 5.5
- Bond, I. A., Udalski, A., Jaroszyński, M., et al. 2004, *ApJ*, 606, L155 1
- Bramich, D. M. 2008, *MNRAS*, 386, L77 3.3, 5.2

- Carroll, B. W. & Ostlie, D. A. 2006, *An introduction to modern astrophysics and cosmology* (Institute for Mathematics and Its Applications)
- Cassan, A. 2008, *A&A*, 491, 587 2.5
- Cassan, A., Beaulieu, J. P., Brilliant, S., et al. 2004, *A&A*, 419, L1 5.1
- Cassan, A., Beaulieu, J.-P., Fouqué, P., et al. 2006, *A&A*, 460, 277 5.1
- Castro, S., Pogge, R. W., Rich, R. M., DePoy, D. L., & Gould, A. 2001, *ApJ*, 548, L197 5.1
- Chwolson, O. 1924, *Astronomische Nachrichten*, 221, 329 2.2
- Claret, A. 2000, *A&A*, 363, 1081 2.8.1, 5.3, 5.7, 5.4
- Dominik, M. 2004, *MNRAS*, 352, 1315 5.3
- Dominik, M. 2006, *MNRAS*, 367, 669 5.4.3
- Dong, S., Bond, I. A., Gould, A., et al. 2008, *ArXiv e-prints* 4.2
- Ehrenreich, D., Lecavelier des Etangs, A., Beaulieu, J.-P., & Grasset, O. 2006, *ApJ*, 651, 535 4.1
- Einstein, A. 1936, *Science*, 84, 506 2.2, 5.4.1
- Eisenhauer, F., Genzel, R., Alexander, T., et al. 2005, *ApJ*, 628, 246 5.5
- Fields, D. L., Albrow, M. D., An, J., et al. 2003, *ApJ*, 596, 1305 5.1
- Gaudi, B. S., Bennett, D. P., Udalski, A., et al. 2008, *Science*, 319, 927 4.1
- Gaudi, B. S. & Sackett, P. D. 2000, *ApJ*, 528, 56 4.3.1
- Gould, A. 1994, *ApJ*, 421, L71
- Gould, A. & Loeb, A. 1992, *ApJ*, 396, 104 4.1
- Gould, A., Udalski, A., An, D., et al. 2006, *ApJ*, 644, L37 4.2
- Griest, K. & Safizadeh, N. 1998, *ApJ*, 500, 37 4.2
- Groenewegen, M. A. T. 2004, *MNRAS*, 353, 903 5.5
- Groenewegen, M. A. T. 2008, *A&Aaccepted*, *ArXiv/0807.2764* 3.4, 5.5
- Groenewegen, M. A. T., Udalski, A., & Bono, G. 2008, *A&A*, 481, 441 5.5
- Gustafsson, B., Bell, R. A., Eriksson, K., & Nordlund, A. 1975, *A&A*, 42, 407 5.6
- Gustafsson, B., Edvardsson, B., Eriksson, K., et al. 2008, *ArXiv e-prints*, 805 5.1, 5.6
- Gustafsson, B., Edvardsson, B., Eriksson, K., et al. 2003, in *Astronomical Society of the Pacific Conference Series*, Vol. 288, *Stellar Atmosphere Modeling*, ed. I. Hubeny, D. Mihalas, & K. Werner, 331–+ 5.6

- Hendry, M. A., Coleman, I. J., Gray, N., Newsam, A. M., & Simmons, J. F. L. 1998, *New Astronomy Review*, 42, 125 5.1
- Heyrovský, D. 2003, *ApJ*, 594, 464 5.1, 5.4.1, 5.7, 5.8, 5.8
- Heyrovský, D. 2007, *ApJ*, 656, 483 5.7, 5.4
- Heyrovsky, D. 2008, in "Introduction to Microlensing", in *Proceedings of the Manchester Microlensing Conference: The 12th International Conference and ANGLES Microlensing Workshop*, eds. E. Kerins, S. Mao, N. Rattenbury and L. Wyrzykowski. Published online at SISSA, *Proceedings of Science.*, p.28 5.1, 5.8, 5.6
- Heyrovský, D., Sasselov, D., & Loeb, A. 2000, *ApJ*, 543, 406 5.1
- Houdashelt, M. L., Bell, R. A., Sweigart, A. V., & Wing, R. F. 2000, *AJ*, 119, 1424 5.5, 5.6
- Jiang, G., DePoy, D. L., Gal-Yam, A., et al. 2004, *ApJ*, 617, 1307 5.1
- Kains, N., Cassan, A., Horne, K., et al. 2009, *ArXiv e-prints* 3.4, 5.4.2
- Kubas, D., Cassan, A., Beaulieu, J. P., et al. 2005, *A&A*, 435, 941 5.1, 5.3
- Kubas, D., Cassan, A., Dominik, M., et al. 2008, *A&A*, 483, 317 5.8
- Kupka, F., Piskunov, N., Ryabchikova, T. A., Stempels, H. C., & Weiss, W. W. 1999, *A&AS*, 138, 119 5.6
- Kurucz, R. 1994, *Solar abundance model atmospheres for 0,1,2,4,8 km/s*. Kurucz CD-ROM No. 19. Cambridge, Mass.: Smithsonian Astrophysical Observatory, 1994., 19 5.7
- Kurucz, R. L. 1992, in *IAU Symposium, Vol. 149, The Stellar Populations of Galaxies*, ed. B. Barbuy & A. Renzini, 225–+ 5.1, 5.7, 5.8
- Levesque, E. M., Massey, P., Olsen, K. A. G., & Plez, B. 2007, *ApJ*, 667, 202 5.6
- Levesque, E. M., Massey, P., Olsen, K. A. G., et al. 2005, *ApJ*, 628, 973 5.6
- Loeb, A. & Sasselov, D. 1995, *ApJ*, 449, L33+ 5.1
- Mao, S. & Paczyński, B. 1991, *ApJ*, 374, L37 1, 4.1
- Massey, P., Levesque, E. M., Plez, B., & Olsen, K. A. G. 2008, *ArXiv e-prints*, 801 5.6
- Paczynski, B. 1986, *ApJ*, 304, 1 2.5, 5.1, 5.4.1
- Paczynski, B. 1996a, *ARA&A*, 34, 419 2.3, 2.4
- Paczynski, B. 1996b, in *IAU Symposium, Vol. 173, Astrophysical Applications of Gravitational Lensing*, ed. C. S. Kochanek & J. N. Hewitt, 199–+
- Paczynski, B. & Stanek, K. Z. 1998, *ApJ*, 494, L219+ 3.4, 5.5
- Plez, B. 1998, *A&A*, 337, 495 5.6

- Plez, B., Brett, J. M., & Nordlund, A. 1992, *A&A*, 256, 551 5.1, 5.6
- Plez, B., van Eck, S., Jorissen, A., et al. 2003, in *IAU Symposium*, Vol. 210, *Modelling of Stellar Atmospheres*, ed. N. Piskunov, W. W. Weiss, & D. F. Gray, 2P+ 5.6
- Press, W. H., Teukolsky, S. A., Vetterling, W. T., & Flannery, B. P. 1992, *Numerical recipes in C. The art of scientific computing* (Cambridge: University Press, —c1992, 2nd ed.) 3.3.2
- Rattenbury, N. J., Bond, I. A., Skuljan, J., & Yock, P. C. M. 2002, *MNRAS*, 335, 159 4.2
- Refsdal, S. 1964, *MNRAS*, 128, 307
- Sasselov, D. D. 1996, in *Astronomical Society of the Pacific Conference Series*, Vol. 109, *Cool Stars, Stellar Systems, and the Sun*, ed. R. Pallavicini & A. K. Dupree, 541+ 5.1
- Stanek, K. Z. & Garnavich, P. M. 1998, *ApJ*, 503, L131+ 3.4, 5.5
- Strassmeier, K. G. & Schordan, P. 2000, *Astronomische Nachrichten*, 321, 277 5.6
- Sumi, T. 2004, *MNRAS*, 349, 193 5.5
- Thurl, C., Sackett, P. D., & Hauschildt, P. H. 2006, *A&A*, 455, 315 5.1
- Udalski, A. 2003, *Acta Astronomica*, 53, 291 3.1, 4.4, 5.2
- Valls-Gabaud, D. 1995, in *Large Scale Structure in the Universe*, ed. J. P. Mücke, S. Gottloeber, & V. Müller, 326–336 5.1
- Valls-Gabaud, D. 1998, *MNRAS*, 294, 747
- van Belle, G. T., Lane, B. F., Thompson, R. R., et al. 1999, *AJ*, 117, 521
- Walsh, D., Carswell, R. F., & Weymann, R. J. 1979, *Nature*, 279, 381 1
- Witt, H. J. 1990, *A&A*, 236, 311 4.3.2
- Witt, H. J. 1995, *ApJ*, 449, 42 5.1
- Witt, H. J. & Mao, S. 1994, *ApJ*, 430, 505 5.4.1
- Woźniak, P. R. 2000, *Acta Astronomica*, 50, 421 3.3, 4.3.1
- Yoo, J., DePoy, D. L., Gal-Yam, A., et al. 2004, *ApJ*, 603, 139 5.1, 5.4.1

Acknowledgements

I finish my PhD and I would like to acknowledge all the persons that accompanied me in different ways during this particular time: I thank them very much for their help and their presence in my life.

I want to express my acknowledgements to my supervisor Prof. Joachim Wambsganss and thank him for the possibility to gather an interesting experience and for providing financial support.

I would like to thank Prof. Andreas Quirrenbach, Priv.D. Andreas Just and Prof. Ulrich Uwer for agreeing to be the members of my PhD-committee. Priv.D. Christian Fendt for his efforts towards the well-being of us, the International Max Planck Research School PhD-students.

I would like to acknowledge Dr. Arnaud Cassan for his advice, scientific support, experience and help. I would also like to thank everyone else from the PLANET collaboration, in particular, Dr. Pascal Fouqué for his close collaboration regarding data reduction and scientific discussions and Dr. Daniel Kubas and Noé Kains for their advice.

I want to express my acknowledgements to Dr. Szymon Kozłowski for our scientific discussions, for encouraging me and helping me in many aspects of my PhD, as well as Dr. Lukasz Wyrzykowski for interesting scientific discussions.

I want to thank Dr. David Heyrovský for interesting scientific discussions.

I would like to express my acknowledgements to Dr. Atsunori Yonehara, my office mate, for his help and encouragement.

The lensing group at the Astronomisches Rechen-Institut (ARI) in Heidelberg: Dr. Arnaud Cassan, Timo Anguita, Dr. Janine Fohlmeister, Dr. Dominique Sluse, Dr. Robert Schmidt, Christine Liebig, Dr. Cécile Faure, Gabriele Maier, Fabian Zimmer for the companionship, help and the lots of fun we have had together, I want to say: thank you!

I would like to acknowledge Prof. George Melikidze and Marine Margishvili, for their encouragement and support, as well Prof. Janusz Gil for helping me draw the path towards starting this PhD.

Dr. Piotr Amsterdamski and Prof. Roman Juskiewicz were responsible for opening the world of science for me, and for this, I am deeply thankful.

I would like to thank my mother Zofia Samitowska-Zub and father Leslaw Zub, my brothers Roald and Michal for their support in different ways. Mamo, bardzo Ci dziekuje za to, ze jestes, ze mnie wspieralas i za wszystko co dla mnie zrobilas.

I thank very much my IMPRS colleagues for sharing this particular experience and my colleagues from study of astrophysics in Poland: Szymon Kozłowski, Krzysztof Maciesiak, Krzysiek Krzeszowski, Gio Melikidze and Maciej Wojciow.

Finally, I would like to thank all the members of ARI for their goodwill during my stay in Heidelberg.